LUND UNIVERSITY

Structure-Property Relationships of Iron N-Heterocyclic Carbene Complexes

Synthesis, Characterization and Application

Hlynsson, Valtýr Freyr

2024

Document Version:
Publisher's PDF, also known as Version of record

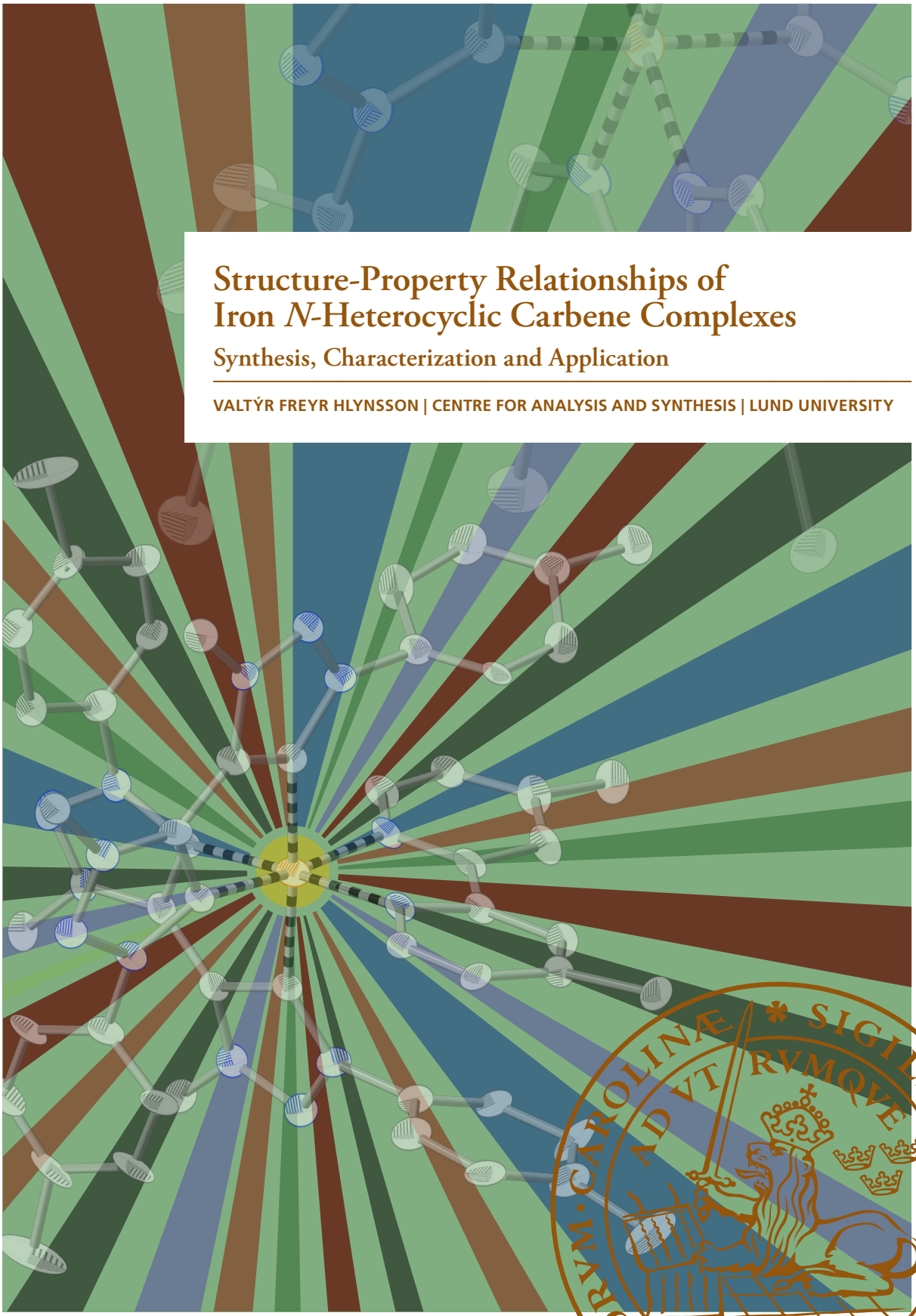

Structure-Property Relationships of Iron *N*-Heterocyclic Carbene Complexes

Synthesis, Characterization and Application

VALTÝR FREYR HLYNSSON | CENTRE FOR ANALYSIS AND SYNTHESIS | LUND UNIVERSITY

Printed by Media-Tryck, Lund 2024 NORDIC SWAN ECOLABEL 3041 0903

LUND UNIVERSITY

ISBN 978-91-8096-020-5

Centre for Analysis and Synthesis
Department of Chemistry
Faculty of Science
Lund University

Structure-Property Relationships of Iron *N*-Heterocyclic Carbene Complexes

Structure-Property Relationships of Iron *N*-Heterocyclic Carbene Complexes

Synthesis, Characterization and Application

Valtýr Freyr Hlynsson

LUND
UNIVERSITY

DOCTORAL DISSERTATION

Doctoral dissertation for the degree of Doctor of Philosophy (PhD) at the Faculty of Science at Lund University to be publicly defended on February 29th, 2024 at 13.00 in Lecture Hall KC:A, Kemicentrum

Faculty opponent
Prof. Mogens Brønsted Nielsen,
Department of Chemistry, University of Copenhagen

Organization: LUND UNIVERSITY

Document name: Doctoral dissertation **Date of issue:** 2024-02-05

Author: Valtýr Freyr Hlynsson

Title and subtitle: Structure-Property Relationships of Iron *N*-Heterocyclic Carbene Complexes: Synthesis, Characterization and Application

Abstract:

Resulting from the general availability of first-row transition metals, compared to their second- and third-row counterparts, photosensitizers (PSs) based on metals like iron have gained interest as candidates to enable photochemistry from solar energy, a largely underutilized energy source. Iron complexes equivalent to other metal complexes, currently being used as PS, do lack some of the advantageous properties required to challenge the established PSs.

In this thesis the investigations on the reactivity and properties of heteroleptic Fe-NHC (*N*-heterocyclic carbene) complexes is described. A group of new complexes have been synthesized and characterized in an attempt to better understand their structure-property relationships and how synthetic design can aid in the search of complexes with properties desired for photochemical applications.

In chapters 2-4 the synthesis of iron complexes, mostly based on previously reported synthesis of heteroleptic Fe-NHC complex, is described. The effects of structural changes in NHC ligands as well as functionalization of 2,2'-bipyridine (bpy) ligands are investigated. Introducing methylene spacers between the NHC units of a bidentate ligand influences the geometry of the complex in an unexpected manner, while functional groups on bpy affect complex properties in a subtle, predictable fashion. For a few of the complexes ground state characterizations reveal that at least two low-energy structural conformations exist in a dynamic equilibrium, slowed down by lowering the temperature. Many of the complexes can be oxidized from oxidation state Fe(II) to Fe(III) by atmospheric oxygen which changes their optical properties.

In the last part of the thesis, application of an Fe-NHC complex as a photoredox catalyst to drive a chemical reaction with green light is presented. While irradiation of lower energy and milder conditions than for conventional methods to catalytically perform the reaction are needed, this photoredox catalyst shows that Fe-NHC complexes can offer value as unconventional photocatalysts. With complexes featuring carboxylic acid anchor groups, photovoltaic performance can now be investigated as well. Its broad absorbance over most of the visible part of the electromagnetic spectrum is promising but rather short excited state lifetime might limit applicability.

Key words: Photoredox catalysis, photovoltaics, photosensitizers, *N*-heterocyclic carbenes, BHAS, synthesis, organometallic chemistry, structure-property relationship, coordination chemistry, heteroleptic iron complexes, geometry, photophysics.

Language English **Number of pages**: 82

ISBN: ISBN 978-91-8096-020-5 (printed)

ISBN 978-91-8096-021-2 (electronic)

Structure-Property Relationships of Iron *N*-Heterocyclic Carbene Complexes

Synthesis, Characterization and Application

Valtýr Freyr Hlynsson

LUND
UNIVERSITY

Front cover by Jóhanna Høeg Sigurðardóttir
Back cover by Jóhanna Høeg Sigurðardóttir and Valtýr Freyr Hlynsson

Faculty of Science
Department of Chemistry
Centre for Analysis and Synthesis

ISBN 978-91-8096-020-5 (printed)
ISBN 978-91-8096-021-2 (electronic)

Printed in Sweden by Media-Tryck, Lund University
Lund 2024

Table of Contents

Popular Science Summary

It is a well known, global problem that non-renewable energy sources are being depleted. Despite social awareness and broad consensus on the need for change, the global energy consumption continues to rise. The transition of global energy systems towards renewable energy needs to happen quicker to avoid further crisis.

The largest source of energy available on Earth is the star of our solar system, the Sun. The temperature on the surface of the Sun is over 5500 °C (temperature of molten lava usually ranges between 800-1200 °C), which is a result of the energy that is generated from the fusion of millions of tons of hydrogen gas into another gas, helium. Every hour, the energy of the sunlight that reaches the Earth would be enough to cover the annual, global energy consumption. The main challenge is to harvest this large and reliable source of energy in a sustainable and efficient fashion.

One method to achieve this goal is to use photosensitizers, molecules that can capture the energy of light to excite an electron into an energetic state. This high-energy electron can then enter a solar cell to create electricity (photovoltaics) or transfer its energy to another molecule that needs the energy to go undergo a chemical reaction (photocatalysis). In both cases, the photosensitizer is recovered in its original state and can continue to capture a new batch of energy.

Many photosensitizers that are being used today are based on extremely rare and expensive, sometimes toxic metals such as ruthenium and iridium. To be able to use photosensitizers globally the materials to make them have to be available.

This thesis describes efforts to design and make new photosensitizers based on iron, of which over one billion tons are produced each year. The performance of iron-based photosensitizers is worse than of those based on precious metals. Strategic design of ligands, molecules that bind to metals to form complexes, can change the nature and improve the performance as photosensitizers.

To successfully design iron complexes that are good enough, understanding of how changes in their structure influences their properties is crucial and what this thesis tries to contribute. Many new iron-complexes, structurally related to allow comparison between them, have been made and carefully investigated. In the final part of the thesis the performance of an iron photosensitizer in photocatalysis is reported, where chemical reaction is driven at conditions greener than is currently done.

List of Papers

This thesis is based on and summarises the following papers:

I. How Rigidity and Conjugation of Bidentate Ligands Affect the Geometry and Photophysics of Iron N-heterocyclic Complexes – A Comparative Study

Om Prakash, Pavel Chábera, Nidhi Kaul, **Valtýr Freyr Hlynsson**, Nils W. Rosemann, Iria Bolaño Losada, Yen Tran Hoang Hai, Ping Huang, Jesper Bendix, Tore Ericsson, Lennart Häggström, Arvind Kumar Gupta, Daniel Strand, Arkady Yartsev, Reiner Lomoth, Petter Persson, Kenneth Wärnmark

In revision

II. Synthesis, Dynamics and Photophysics of Heteroleptic Ferrous and Ferric Complexes Featuring Mesoionic *N*-Heterocyclic Carbene Ligands and Dimethyl-Substituted Bipyridine – A Comparative Study

Valtýr Freyr Hlynsson, Catherine Johnson, Mawuli Deegbey, Arvind Gupta, Zoltan Takacs, Esmaeil Sheibani, Ping Huang, Jesper Bendix, Fredrik Lindgren, Tore Ericsson, Lennart Häggström, Elena Jakubikova, Reiner Lomoth, Kenneth Wärnmark

In manuscript

III. Heteroleptic Ferrous and Ferric Complexes with Mesoionic *N*-Heterocyclic Carbene and Functionalized Bipyridine Ligands – Synthesis and Photophysics

Valtýr Freyr Hlynsson, Pavel Chábera, Catherine Johnson, Arvind Gupta, Zoltan Takacs, Zehan Yao, Nils W. Rosemann, Ping Huang, Jesper Bendix, Fredrik Lindgren, Tore Ericsson, Lennart Häggström, Reiner Lomoth, Petter Persson, Arkady Yartsev, Kenneth Wärnmark

In manuscript

IV. Base-promoted homolytic aromatic substitution (BHAS) reactions and hydrodehalogenations driven by green light and an iron(III)-NHC photoredox catalyst

Lisa H. M. de Groot, **Valtýr Freyr Hlynsson**, Catherine Johnson, Alpesh K. Sharma, Reiner Lomoth, Kenneth Wärnmark

In manuscript

Publications not included in the thesis:

V. HERFD-XANES probes of electronic structures of iron$^{II/III}$ carbene complexes

Meiyuan Guo, Om Prakash, Hao Fan, Lisa H. M. de Groot, **Valtýr Freyr Hlynsson**, Simon Kaufhold, Olga Gordivska, Nicolás Velásquez, Pavel Chábera, Pieter Glatzel, Kenneth Wärnmark, Petter Persson, Jens Uhlig

Phys. Chem. Chem. Phys., 2020, **22**, 9067-9073.

Author's contribution to the papers

Paper I

I performed a significant part of the synthetic work. I wrote large parts of the manuscript and coordinated its finalization and submission. I compiled the supporting information.

Paper II

I performed all synthetic work. I coordinated the collection of all experimental data and prepared samples for NMR analysis, HR-MS analysis and SC-XRD. I took part in and coordinated the data analysis. With input from co-authors, I wrote the manuscript and compiled the supporting information.

Paper III

I performed all synthetic work. I coordinated the collection of all experimental data and prepared samples for NMR analysis, HR-MS analysis, SC-XRD, TAS and photoluminescence measurements. I took part in and coordinated the data analysis. With input from co-authors, I wrote the manuscript and compiled the supporting information.

Paper IV

I performed large parts of the experimental work, including substrate synthesis and characterization, catalyst synthesis, photoredox catalysis and mechanistic investigations. I participated in experimental data analysis and contributed to writing of the supporting information.

Abbreviations

AP	Aldehyde product
BHAS	Base-promoted homolytic aromatic substitution
bpy	2,2'-bipyridine
btz	1,1'-Bis(p-tolyl)-4,4'-bis(1,2,3-triazolium) bis(hexafluorophosphate)
CP	Cyclized product
CT	Charge transfer
DSSC	Dye-sensitized solar cell
EPR	Electron paramagnetic resonance
ES	Excited state
EWG	Electron-withdrawing group
GS	Ground state
HAT	Hydrogen atom transfer
HOMO	Highest occupied molecular orbital
HP	Hydrogen addition product
LED	Light-emitting diode
LF	Ligand field
LMCT	Ligand-to-metal charge transfer
LUMO	Lowest unoccupied molecular orbital
mbmi	1,1'-methylenebis(3-methylimidazol-2-ylidene)
MC	Metal centred
MIC	Mesoionic carbene
MLCT	Metal-to-ligand charge transfer
MO	Molecular orbital
NHC	*N*-Heterocyclic carbene
PC	Photoredox catalyst
PS	Photosensitizer
PV	Photovoltaic

RMSE	Root-mean-square error
SC-XRD	Single-crystal X-ray diffraction
SED	Sacrificial electron donor
SET	Single electron transfer
TEMPO	(2,2,6,6-Tetramethylpiperidin-1-yl)oxyl
TM	Transition metal
TON	Turnover number
tpphz	tetrapyrido[3,2-a:2',3'-c:3",2"-h:2"',3"'-j]phenazine
XAT	Halogen atom transfer

1 Introduction

1.1 Harvesting solar energy

It is a well known, global problem that non-renewable energy sources are being depleted. Despite social awareness and broad consensus on the need for change, the global energy consumption continues to rise. In 2022, fossil fuels represented 82% of the worlds primary energy consumption, steady from year before, while renewables (excluding hydroelectricity) constitute 7.5%, an increase of nearly 1% from the previous year.[1] The transition of global energy systems towards renewable energy, adapting to escalating environmental and geopolitical crises, needs to happen quicker.

The largest energy source available on Earth is the star of our solar system, the Sun. The effective temperature on the surface of the Sun is over 5700 K, which is a result of the energy that is generated from the fusion of millions of tons of hydrogen into helium.[2] The luminosity of the Sun is 383 YJ/s ($383 \cdot 10^{24}$ J/s) and every hour the irradiation that reaches the Earth from the Sun would suffice to cover the annual, global energy consumption (604 EJ in 2022).[1-3] The main challenge is to harvest this vast source of radiant energy in a sustainable and efficient fashion.

1.1.1 Photovoltaics

Photosensitizers (PSs) are molecules that can by absorbing a photon of appropriate energy, which results in the excitation of a charge carrier (electron) into an unoccupied molecular orbital (MO) and take on a higher energy charge transfer (CT) state. If the properties of the excited state (ES), such as lifetime and/or redox potentials, are favorable, the PS, or the system it is a part of, can show photovoltaic (PV) or photocatalytic activity by transferring energy from the ES, while relaxing back to the oxidized ground state (GS). After the PS has been reduced to its original oxidation state, it is ready to start a new cycle by absorbing energy from a new photon. The net result of this simplified event is that energy from light has been absorbed and utilised to perform photochemistry.[4-5]

A PV solar cell is an electrical device that converts radiant energy from the Sun into electricity. There are many types of solar cells based on different material, such as silicon, perovskites, quantum dots and organic molecules, with newer generation

cells being made into thin films or used in tandem techniques.[6] In all of these, the PV effect is exploited to create charge separation and an electric current.

Dye-sensitized solar cells (DSSCs), also known as Grätzel cells,[7-8] are one type of thin-film solar cells that are of relatively low-cost compared to other solar cells. Additionally, DSSCs can be made semi-flexible and semi-transparent which could open up for diverse applications.[6] However, DSSCs carry the disadvantage of their energy conversion efficiency being low compared to other thin-film solar cells. An important and charateristic part of the DSSC is the PS. In the DSSC PV system, the excited PS (PS*) interacts with a semiconductor surface in a redox event where an electron is transferred. This charge separation results in an electronic current, where the electron is transported into the semiconductor bulk, through an electrical circuit to the counter electrode. In an n-type system, the oxidized PS accepts an electron from an electrolyte (for example I^-/I_3^-), which is reduced at the counter electrode, thereby regenerating the PS to its GS and completing the redox cycle (Figure 1).[9-10]

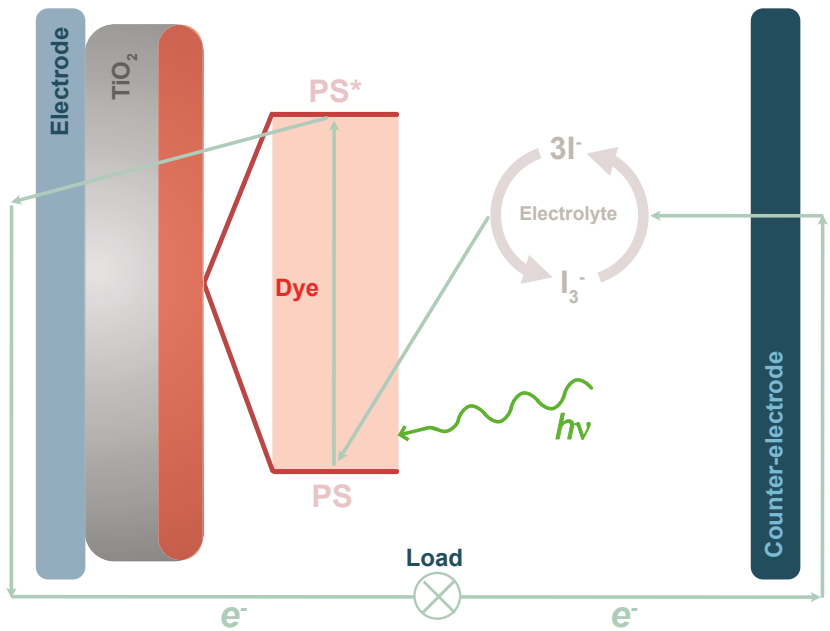

Figure 1 A schematic overview of the operational principle of an n-type DSSC.

1.1.2 Fe vs. Ru Photosensitizers

Many of the highest performing DSSCs today are based on PSs containing noble metals that are scarce and expensive, such as ruthenium (**1**)[11] and iridium (**4**)[12] (Figure 6). The estimated total amount available on Earth (~1 x 10^{-7}% of the mass of Earth's crust)[13] is insufficient to sustain a world-wide application of solar cells

based on these metals. To address this, the element above ruthenium in the periodic table, iron, has been put forward as a potential replacement. Considering its vast supply (>5% of the mass of Earth's crust)[13] and comparatively benign properties, iron has the potential to be suitable for applications in commercial solar cells.

In the case of Ru-based PSs, prevalent in the field, the time that an excited electron populates an ES before it relaxes back to the GS (ES lifetime, τ) is comparatively long (μs).[14] This increases the likelihood of the high-energy electron taking part in a photochemical event, such as an energy transfer to a substrate in order to photocatalytically facilitate a chemical reaction. First-row TMs, including iron, share the intrinsic attribute of a weaker ligand field (LF) than second- and third-row TMs. This fundamental difference can be explained by the primogenic effect, which predicts weaker metal-ligand orbital overlap (weaker bonding) when 3d orbitals are involved (first-row TMs) since they lack radial nodes in their d-orbital wave functions, resulting in the contraction of the d-orbitals.[15-17] The implications for such complexes are metal centered states ($^{3/5}$MC) which are relatively low in energy, compared to their isoelectronic second- and third-row counterparts, facilitating the non-productive deactivation of an electron from a CT state, thereby limiting their photochemical application (Figure 2).[17]

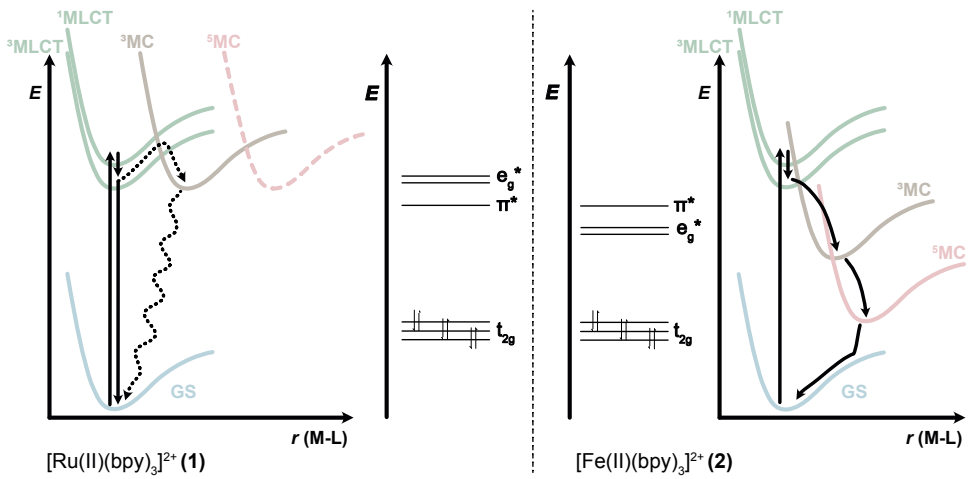

Figure 2 An overview of the energy transitions and electronic states of Ru and Fe polypyridyl complexes **1** (left) and **2** (right), following a photoexcitation event, and molecular orbital diagrams of the frontier orbitals involved in the photoexcitation of **1** and **2**.

1.1.3 The electronic structure of Fe photosensitizer

To circumvent or solve the inherent problem with Fe complexes, several strategies to, through strategic ligand design, manipulate the energy of the electronic states have been proposed and investigated.[14, 18]

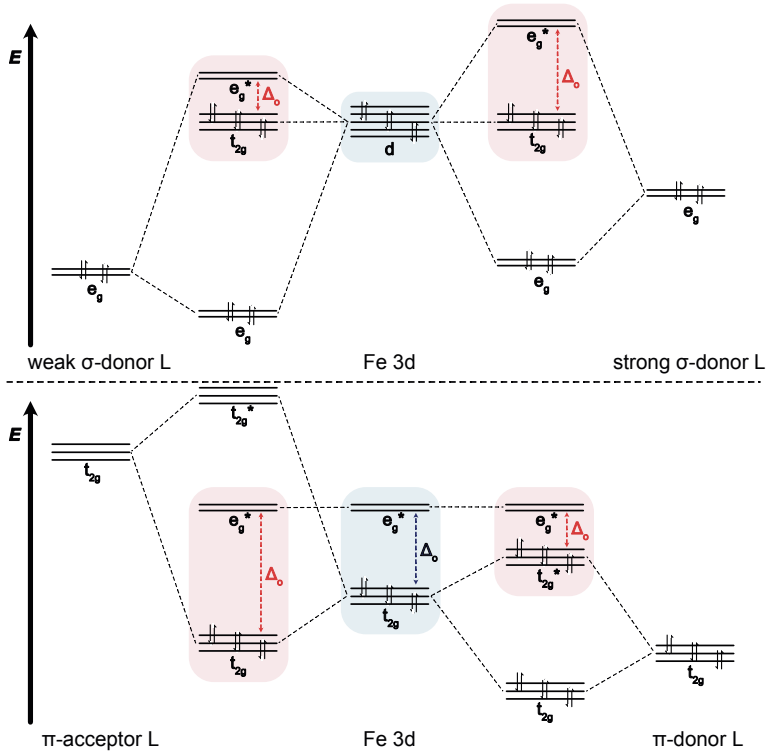

Figure 3 Orbital diagrams showing the effect of bonding interactions between metal d orbitals and ligand orbitals on ligand field splitting (Δ_o).

The introduction of strongly σ-donating ligands to replace polypyridyl ligands, which are conventionally used in photochemistry, has been shown to be highly effective in raising unpopulated MC states in energy by strengthening the ligand field induced on Fe (Figure 3, top). This can hamper the unproductive deactivation of the excited electron and increase the likelihood of a photochemically productive event occurring. *N*-heterocyclic carbenes (NHCs, Figure 4) are a group of persistent carbenes. Their stability is attributed to electron density donated from heteroatoms (typically nitrogen) to the unpopulated p-orbital of the carbene carbon. Upon coordination to a metal, the free electron pair (NHCs are singlet carbenes) of the carbene carbon is the main contributor to the electron density that is donated to the metal.

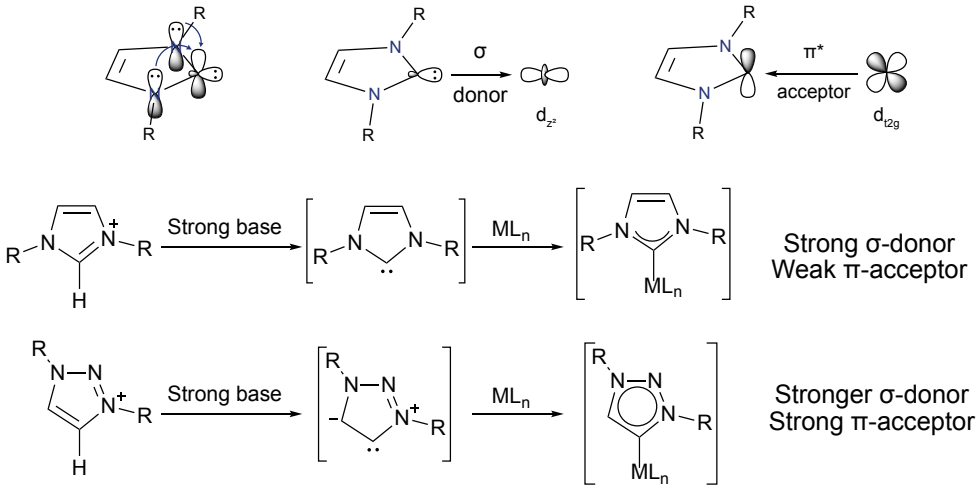

Figure 4 Top left: Orbital explanation for the stability of NHCs. Top centre: σ-donation from a carbene lone pair to a metal orbital. Top right: π-accepting of the carbene from a filled d (d_{xy} / d_{xz} / d_{yz}) orbital on the metal. Imidazolium salt (centre row) and triazolium salt (bottom row) carbene precursors, deprotonated by a strong base to yield the free N-heterocyclic carbene (NHC) and mesoionic carbene (MIC), respectively. They can effectively coordinate to metals.[19-24]

Numerous Fe-NHC complexes have been reported where it has been shown that the coordination of NHC ligands significantly improves photophysical properties and ES lifetimes of the complexes and the improvement is proportional to the number of coordinated NHC units.[25-26] However, when the σ-donation is large enough, the oxidized d^5 Fe(III) GS is stabilized to a point where the single electron oxidation (by atmospheric O_2) from Fe(II) to Fe(III) is a favorable process. This changes the ES dynamics, since the t_{2g} orbital set in the case of an Fe(III) complex has an unpaired electron, which leads to a ligand-to-metal CT (^{2}LMCT) state, in contrast to the metal-to-ligand CT (^{1}MLCT/^{3}MLCT) states found for d^6 complexes (Figure 5).[27-29]

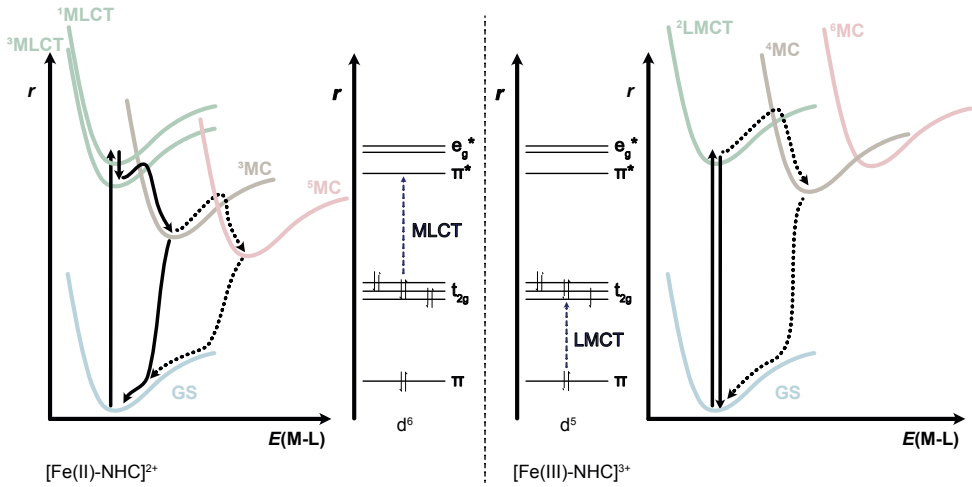

Figure 5 An overview of the energy transitions and electronic states of generic Fe(II)-NHC (d^6) complexes (left) and Fe(III)-NHC (d^5) complexes (right),[18, 28, 30-32] following a photoexcitation event, and molecular orbital diagrams showing their metal-to-ligand charge transfer (MLCT) and ligand-to-metal charge transfer (LMCT) electronic transitions, respectively.[31]

In addition to the number of NHC units coordinated to the iron core, there are other factors that can be manipulated to further alter the electronic structure and photophysical properties of iron complexes. Through strategic ligand design, the LF strength, and subsequentially the relative energy of the MC states can be modified by adjusting the geometry of the coordination sphere, where a higher degree of octahedricity translates to a stronger LF.[33-34] However, the effect of octahedricity on the LF strength is generally less pronounced than the effect of NHC σ-donation.[25-26, 28, 33-34]

The ES dynamics of Fe-based PSs can be tuned further by altering the molecular and electronic structure of the ligands. Small changes can be achieved by modifying the electron density and donation of the NHC unit to affect the energy of the MC states. Changing the ligand nature also influences the energy and geometry of ligand-based MOs and as a result, the energies of orbitals involved in electronic transitions (HOMO/LUMO). The relative energies of the ligand-based orbitals that have π-symmetry are affected by the electron density of the π-system, where it influences the ability to form π-bonds to the metal (Figure 3, bottom).[18, 35]

A common ligand functionalization, especially if the properties of complexes for PV applications are to be investigated, is to introduce so-called anchoring groups. They are employed as linking groups to attach (sensitize) PS to semiconductor surfaces (Figure 6). The most common anchoring group is the carboxylic acid, which not only acts as a linker, but also as an electron-withdrawing group (EWG),

thereby influencing the electron density of its ligand π-system and the LF of the metal (Figure 3, bottom).[9-10]

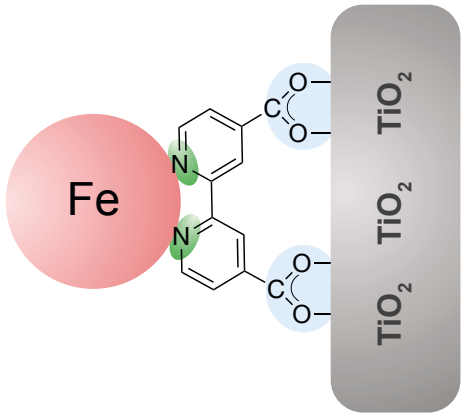

Figure 6 Schematic representation of an Fe-based chromophore adsorbed to a semiconductor (TiO_2) surface through a pair of carboxylic acid (COOH) anchoring groups.

1.1.4 Photoredox catalysis

In addition to the PV applications, PSs can also be employed as photoredox catalysts (PCs), Figure 7.[11-12, 36-38] In photoredox catalysis the excited electron participates in a single electron transfer (SET) event between the PC and a reaction component, where photonic energy is employed to generate highly reactive intermediates of radical character to facilitate a chemical reaction.[39-40]

Certain properties are beneficial for efficient catalysis. The PC should exhibit absorption of visible light, preferably where other reaction components do not absorb. In addition, the generated ES should be long-lived enough to participate in a SET. The SET between a PC and an electron donor or acceptor is facilitated by matching ES redox potentials. Furthermore, the oxidation or reduction of the PC should be reversible so that the PC GS can be regenerated and degradation of the PC, avoided. A PC should also be photostable, as the ability to withstand prolonged irradiation can lead to higher turnover numbers (TON).[41]

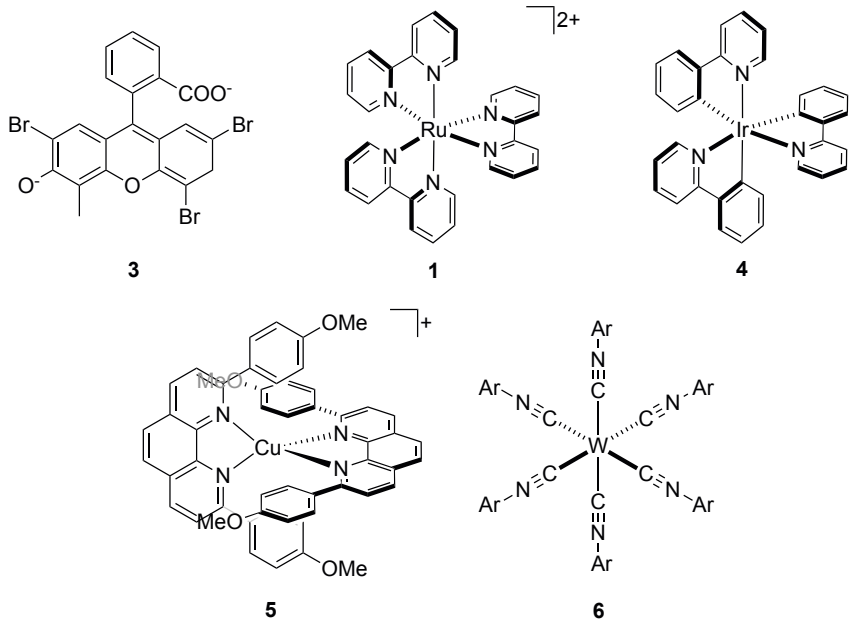

Figure 7 Examples of known photoredox catalysts (PCs).[11-12, 36-38] Ar = diisopropylphenyl (dipp) moiety featuring varying substituents.

Upon irradiation, the PC* can be quenched through SET, either reductively by accepting an electron from an electron donor or oxidatively by reducing an electron acceptor. The SET is bimolecular and for it to take place, the two species (PC* and electron acceptor/donor) must diffuse towards each other. After the SET, the resulting species must diffuse away from each other, out of the solvent cage, to avoid an unwanted back reaction. The quenching of PC* and cage escape is followed by a second SET step to recover the PC to its original oxidation state, closing the catalytic cycle (Figure 8).[11, 40-42]

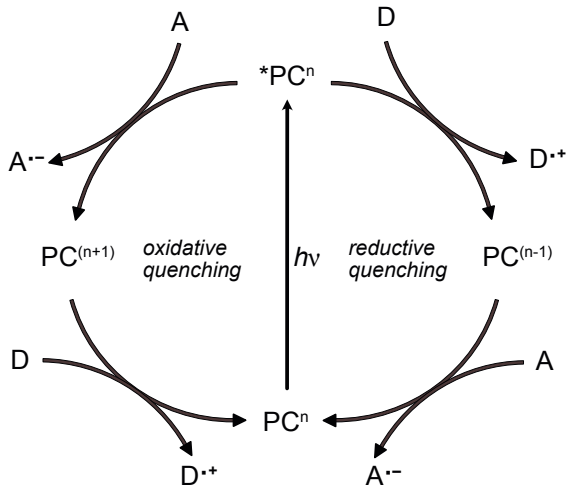

Figure 8 Schematic overview of oxidative and reductive quenching photoredox catalytic cycles. PC = Photoredox catalyst, D = electron donor, A = electron acceptor.

1.2 Synthesis of Fe-NHC complexes

As carbenes, NHCs in their free state are reactive compared to many other ligand types.[19] Even if they are considered persistent carbenes, they are still quite reactive and cannot always be isolated. They have a strong tendency to form C-C bonds through dimerization. For that reason, during synthesis of an NHC-Fe complex, the carbenes are generated in situ by deprotonation, followed by addition of the metal source, normally at reduced temperatures.[25, 28] This carbene generation introduces an additional deprotonation step compared to making traditional TM-complexes bearing polypyridine ligands, which can be obtained relatively easily by the mixing of ligands and a TM precursor.[43] Alternatively, the carbene can be generated and coordinated to a TM through transmetalation via a carbene transfer agent, such as Ag(I) salts. Ag_2O can act as a base to deprotonate the carbene precursor and subsequently coordinate the NHC. The coordination to Ag is relatively weak and the NHC can undergo transmetalation to a different TM, allowing stronger coordination.[44]

Many NHC ligands are tridentate, meaning that there are three interactions between metal d-orbitals and ligand-based orbitals, located on covalently bound atoms. There are two kinds of tridentate ligands, which differ in the way the three units are connected; a tripodal (scorpionate) type[28] and a chelating (pincer) type[27] (Figure 9, top). The former occupies three coordination sites on one face of the metal (facial), with each unit being connected to a common center. The latter coordinates one side

of the metal in a meridional fashion, with the three units being sequentially connected, forming a "pincer" around the metal.

NHC ligands can also be bidentate, where three ligands are needed to fill the coordination sphere of an octahedral complex. Complexes with such ligand stoichiometry can have two enantiomers, the "left-handed screw" (Λ) and the "right-handed screw" (Δ) (Figure 9, bottom).

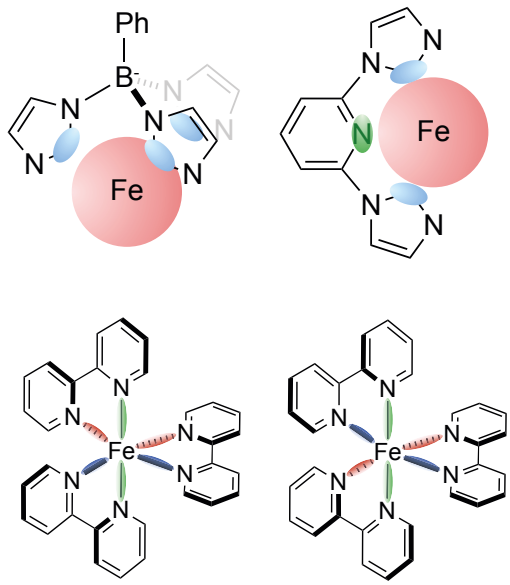

Figure 9 Top: Tripotal and chelating type tridentate ligands. Bottom: **Λ-2** and **Δ-2** exemplifying the two enantiomers available for complexes bearing bidentate ligands.

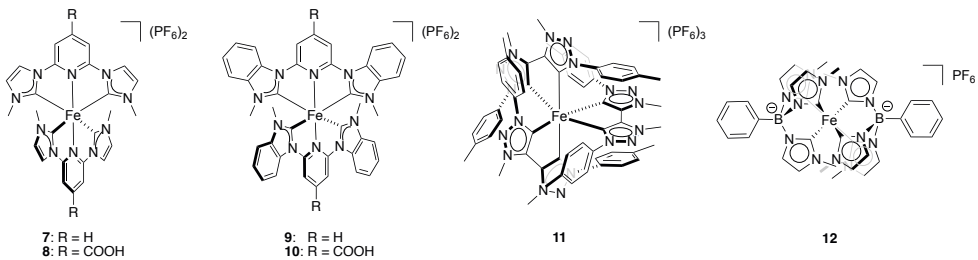

Figure 10 Selected examples of homoleptic Fe-NHC complexes.[27-28, 30, 35, 45]

The complexes shown in Figure 10 have in common that they are homoleptic, i.e. all coordinated ligands are identical. When two or more structurally different ligands coordinate the metal center, the complex is conversely termed heteroleptic (Figure 11). Synthetically, obtaining a heteroleptic complex is often more challenging than

a homoleptic one. For example, different ligands can have unequal affinity for the metal, demanding additional synthetic steps or strategies to avoid the exclusive formation of homoleptic complexes or statistical mixtures of complexes. The latter can be a viable strategy, especially when more than one of the complexes from the reaction mixture are of interest, provided that they can be separated and isolated.[46]

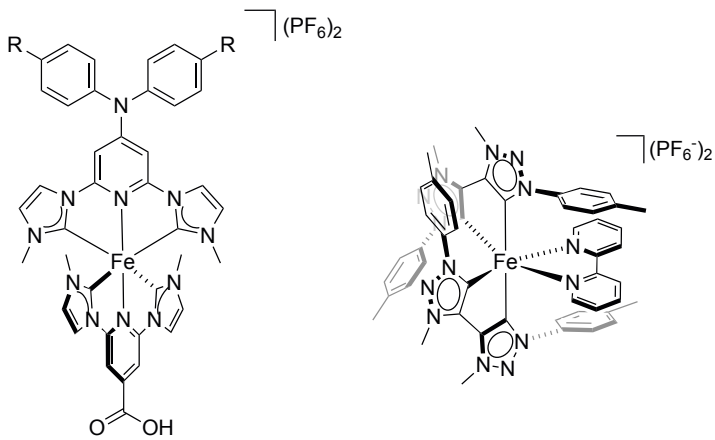

12: R = Me
13: R = OMe

14

Figure 11 Selected examples of heteroleptic Fe-NHC complexes [25, 46]

The synthesis of heteroleptic complex **14** (Scheme 1)[25] showcases the stepwise process to obtain a heteroleptic complex. A single 2,2'-bipyridine (bpy, **15**) ligand was coordinated to $FeCl_2$ in EtOH, giving the high-spin complex [Fe(bpy)Cl_2] (**16**), which precipitates out of the solution as a bright orange powder. Care has to be taken when handling intermediate **16**, since it will easily form the homoleptic, thermodynamically stable **2**.[47] Therefore, the only purification performed on **16** was filtration and washing with EtOH. In THF, the so-obtained **16** was treated with excess of the NHC-ligand 1,1'-Bis(p-tolyl)-4,4'-bis(1,2,3-triazolium) bis(hexafluorophosphate) (btz, **17**) and *t*-BuOK as base to fill the coordination sphere of Fe. It is important to coordinate the pyridyl ligand first, because the chelating **17** ligands are inert to disassociation after coordination, meaning that the homoleptic complex **11** will be the main product if **17** is added before or at the same time as any pyridine-based ligand.[25]

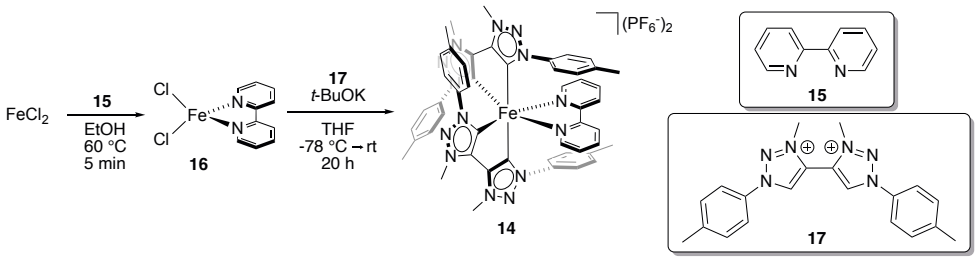

Scheme 1 Synthesis of heteroleptic Fe(II)-NHC complex **14** from $FeCl_2$.[25]

1.3 Aim of this thesis

This thesis describes the synthesis of Fe-NHC complexes and efforts to understand their structure-property relationships and evaluate applicability as PS for photochemical purposes.

Synthesis of iron coordination complexes requires good control over ligand stoichiometry, especially when it comes to heteroleptic complexes. In Chapters 2-4 syntheses of various homo- and heteroleptic iron (and cobalt) complexes are described

First-row TMs share the intrinsic attribute of weaker LF than second- and third-row TMs, resulting in fast, non-productive deactivation of electrons in ESs which limits their photochemical application. Strongly σ-donating NHC-ligands can influence the electronic structure of iron complexes to counteract the deactivation problem and extend ES lifetimes. To gain systematic understanding of the factors that influence important properties of Fe-NHC complexes and how they can be affected through strategic synthetic design, careful characterization and analysis of structure and properties of complexes is crucial. In Chapter 3-4 new Fe-NHC complexes are characterized and compared to relevant, previously reported complexes.

Finally, to evaluate if the improved photophysical properties of new generations of Fe-NHC complexes translate to functioning PS, Chapter 5 describes the application of an Fe-NHC complex as a PC in a photocatalytical system that drives a chemical reaction.

2 Towards the synthesis of binuclear photosensitizer-catalyst complex

2.1 Background

As previously mentioned, a PS can capture photonic energy by exciting an electron, forming PS*. The ES can then partake in a SET event to or from the PS. If the PS exhibits photoredox catalytic activity it is referred to as a PC. If the photoredox catalytic activity of a PS is hampered, an external catalyst can be used along with an electron relay to form a three-component photoredox catalytic system.[48-50] The electron transfer can be bimolecular, but more efficient electron transfer can be achieved by bringing the different components together with a conjugated, molecular linker, making the electron transfer intramolecular. The linker can act as the relay and as an electron reservoir if needed.[51]

Binuclear complex **18** (Figure 12), reported by Canton et al., consists of a Ru-based photosensitizer linked to a Co-based PC, through a tetrapyrido[3,2-a:2',3'-c:3",2"-h:2"',3"'-j]phenazine (tpphz, **19**) ligand.[51] The linker can be viewed as two 1,10-phenanthroline (phen, **20**) ligands linked by a pyrazine unit, chelating to metals on each side. The electron transfer following the photoexcitation of ruthenium through the conjugated linker to reduce the Co-moiety was investigated in an attempt to understand the structure-function relationship of the electron transfer.

In this chapter, the attempted synthesis of $[(btz)_2Fe(II)(tpphz)Co(III)(bpy)_2](PF_6)_5$ (**21**, Figure 12) is described. Most of the experimentation revolved around obtaining the $[Fe(btz)_2(N\text{-}N')]^{2+}$ (analog of **14**, Scheme 1) part of **21**.

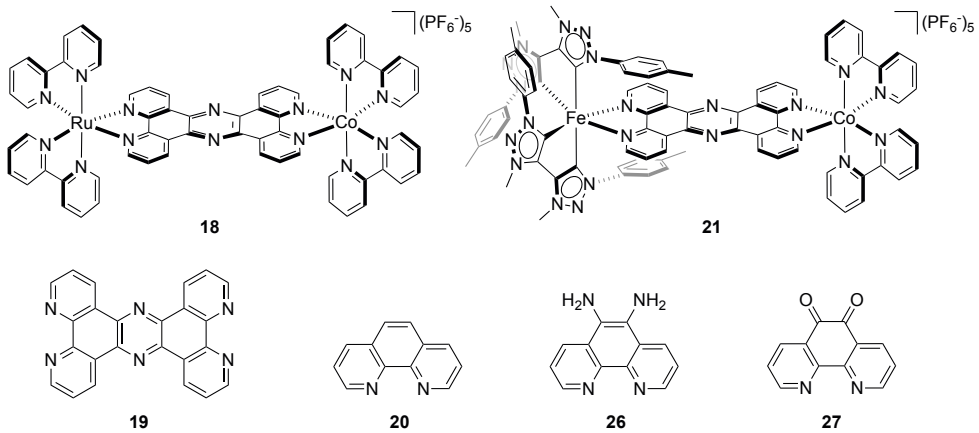

Figure 12 Molecular structures of bimetallic Ru-Co complex **18**[51] and its analog, Fe-Co complex **21**, the synthetic target of this project. The tpphz ligand **19** along with two 1,10-phenanthroline (**20**) derivatives (**26**-**27**) that it can be made from.

2.2 Attempted synthesis

Inspired by binuclear complex **18**, complex **21** was designed where the Ru-based PS is replaced with a Fe-NHC PS, based on previously published Fe-NHC complex **14**. Based on the reported synthesis of **18** (Scheme 2), where $[Ru(bpy)_2(tpphz)](PF_6)_2$ (**22**) and *cis*-$[Co(bpy)_2(OTf)_2]OTf$ (**23**) are refluxed together,[51] our initial synthetic strategy was based on the synthesis of $[Fe(btz)_2(tpphz)](PF_6)_2$ (**24**). Applying a similar synthetic strategy as was used for complex **14**,[25] $FeCl_2$ was first treated with ligand **19** in EtOH. Unfortunately, most likely due to the poor solubility of the large conjugated ligand in the solvent, no observed $[Fe(tpphz)Cl_2]$ (**25**) was observed. The next strategy was based on the fact that ligand **19** can be made through the condensation of 5,6-diamino-1,10-phenanthroline (**26**) and 1,10-phenanthroline-5,6-dione (**27**). Both of these derivatives of **20** have higher, although not high, solubility in EtOH than **19** and when they were separately heated with $FeCl_2$ in such a solution, both resulted in the formation of an unknown solid. Since isolation of the desired $[Fe(phen)Cl_2]$ derivatives **28** and **29** (Scheme 2) can be challenging, each solid was treated with NHC-ligand **17** in THF in an attempt to obtain complexes **30** and **31** (Scheme 2). The plan was to perform the tpphz condensation with either **26** or **27** being coordinated to Fe. These experiments were never carried out, since neither **30** nor **31** could be identified in their respective reaction mixtures. As discussed in Chapter 1 the Fe complex coordinated by three chelating bidentate ligands ($[Fe(N\text{-}N')_3]^{2+}$, (N-N': phen/bpy)) is thermodynamically favored over the monocoordinated Fe complexes[47] (here **28** and **29**) and therefore the solids obtained from the EtOH

solutions most likely contain a mixture of Fe complexes coordinated with two or three of ligands **26** or **27**, as well as other Fe complexes.

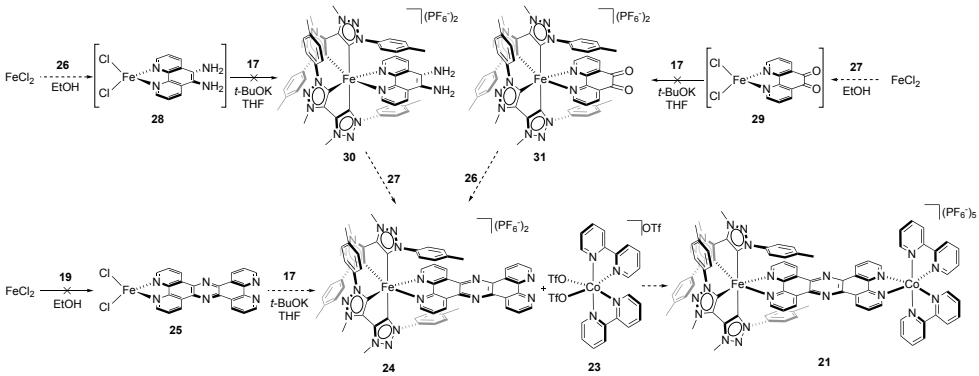

Scheme 2 Attempted synthesis of bimetallic complex **21**.

In an attempt to circumvent the apparent solubility issue of **26** and **27** in EtOH, a different pathway to **28** or **29** was explored. The polynuclear complex $Fe_4Cl_8(THF)_6$ (**32**) can be isolated as a solid after a reaction of $FeCl_3$ with metallic Fe in THF.[52] In the crystal structure (Figure 13), two distinct coordination environments can be seen for Fe, trigonal bipyramidal and octahedral, while there are three types of Cl ligand (μ_1-Cl (terminal), μ_2-Cl and μ_3-Cl). Brechin reported that **32** coordinates one **27** ligand to give **29**, when mixed in DCM.[53] It was also noted that choice of reaction medium is crucial to suppress the formation of $[Fe(phen)_3]^{2+}$, which echos our experience with **16** and derivatives. Judging from the color of the formed precipitate, matching what is described in the procedure,[52] cluster **32** was successfully formed. Unfortunately, all our attempts to coordinate a single phen or bpy ligand to form a $[FeCl_2(N\text{-}N')]$ (N-N': phen/bpy) complex failed.

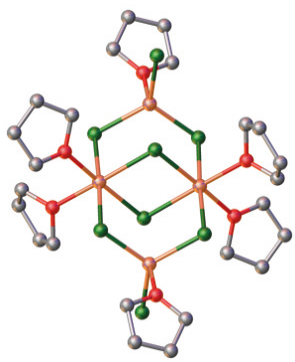

Figure 13 Crystal structure of $Fe_4Cl_8(THF)_6$ cluster **32**.[52] Gray: C atom; Red: O atom; Orange: Fe atom; Green: Cl atom. Hydrogen atoms are omitted for clarity.

Following the reported experimental procedure from the synthesis of **18**, **23** was made from $CoCl_2$ through oxidative coordination of **20**, with Cl_2 gas, followed by ligand substitution/counterion exchange (Scheme 3).[51] However, since the Fe equivalent of **22** was not obtained, the final reaction to combine the Fe and Co parts could not be attempted. Instead, options to coordinate **19**, or its parts (**26** or **27**), to Co were investigated, aiming to coordinate the full $[Co(bpy)_2tpphz]^{3+}$ (**33**) complex to $FeCl_2$ and completing the synthesis of complex **21** by coordination of two carbene NHC ligands **17**. With $[Co(bpy)_2Cl_2]Cl$ (**34**) and **23** in hand, a two-step procedure adapted from the reported synthesis of $[Co(phen)_2tpphz]^{3+}$ (**35**)[54] was attempted on each of the Co complexes **23** and **34**. Unfortunately, none of the reactions were successful. To investigate the reproducibility of the reported procedure,[54] complex $[Co(phen)_2Cl_2]Cl$ (**36**) was made through the same procedure as for **34**.[53] Unfortunately, the attempted coordination of **27** to **36** in refluxing EtOH/water mixture did not yield the desired complex.

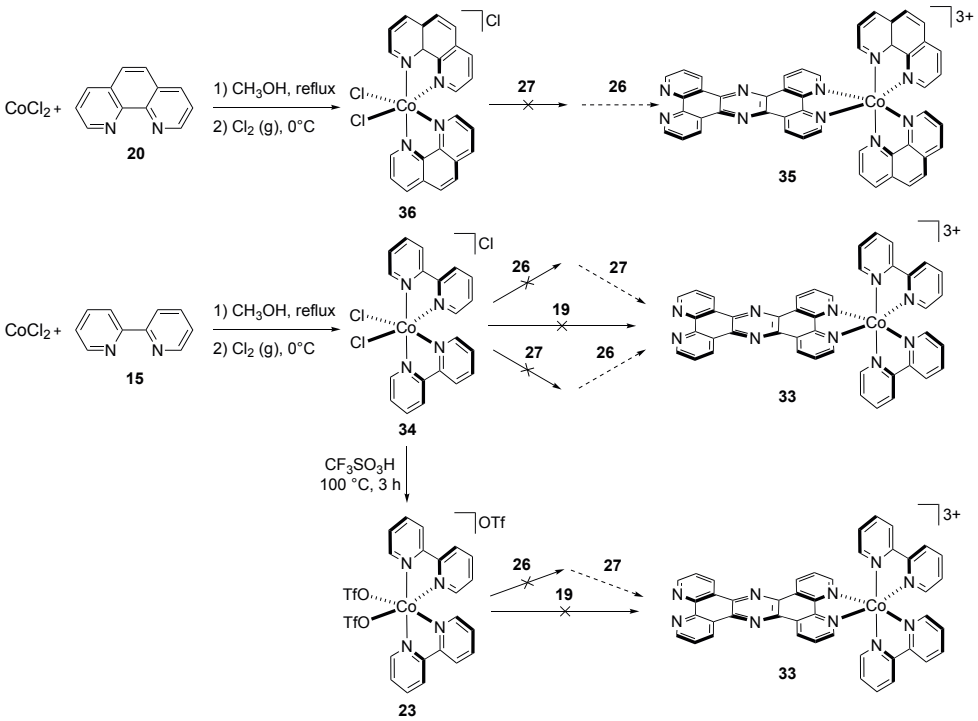

Scheme 3 Attempted syntheses of Co complexes **33** and **35**.[54]

2.3 Conclusion

In this chapter, attempts towards the synthesis of binuclear complex **21** has been described. Complex **21** consists of a Fe-NHC-based PS which is linked to a Co-based PC through a linker. The synthesis of previously reported binuclear complex **18** was used as a reference in the early stages of the project.[51] It soon became clear that the coordination chemistry of iron is more complicated than that of ruthenium and that synthetic adjustments would have to be made.

Synthetic strategies based on the mono coordination of linker ligand **19** (or parts of it) to iron failed, owing to either poor ligand solubility in EtOH or the thermodynamic driving force to fill the coordination sphere of Fe with phenanthrene-type ligands. Even attempting a reported procedure to obtain a mono-phenanthroline Fe complex (**25**, **28** or **29**), going from Fe-cluster **32** failed.

The Co part of **21** was successfully synthesized. Due to the issues with synthesis of the Fe half containing the linker ligand, attempts were made to instead first introduce linker **19** to Co before attempting coordination to Fe. Unfortunately, these attempts were also unsuccessful.

Despite the failure to obtain the target binuclear complex **21**, the attempted synthetic strategies provided valuable information and experience about limits and possibilities of this type of chemistry, which was put to use in the work described in the following chapters.

3 The effect of ligand structure on geometry and photophysics of Fe-NHC complexes (Paper I)

3.1 Background

One of the strategies to extend ES lifetimes of iron complexes and make them viable for photochemical applications is to increase the LF strength by making the geometry of the coordination sphere more octahedral, which can be achieved through strategic ligand design.[33-34, 55-61] The increased LF strength is the result of better overlap between the relevant molecular orbitals of the ligands and the metal d-orbitals. Two complexes previously reported by our group (**11**[27] and **14**[25], Figure 15) both feature the bidentate, mesoionic carbene (MIC) ligand **17**. Complex **11** is a homoleptic Fe(III) complex with three **17** ligands, while **14** is a heteroleptic Fe(II) complex with two **17** ligands and a single **15** ligand.

Ligand **17** is bidentate, with two triazolium MIC units capable of coordinating a metal upon deprotonation by a base. MICs are so-called since their free form does not have a resonance form without formal charges. In the case of **17**, one resonance form has a formal negative charge on the carbene C, making it a stronger σ-donor than the normal NHC. Additionally, they are stronger π-acceptors than regular NHCs, owing to the increased number of N atoms lowering the energy of their π* orbitals.[14, 62] **17** has a rigid, planar structure and the relatively close proximity of the two carbene moieties limits the bite angle when coordinated to a metal. Despite this limitation, the homoleptic complex **11** is highly symmetric and exhibits *trans*-C-Fe-C bond angles of 179°,[27] close to the ideal octahedral angle of 180°. However, the interligand C-Fe-C angles are found further away from the ideal 90° for octahedral complexes.

NHC ligand 1,1'-methylenebis(3-methylimidazol-2-ylidene) (mbmi, **39**) is bidentate, where the NHC units are based on imidazolium and separated by a methylene unit (Figure 15). Introducing spacers between NHC carbene units has been shown to improve octahedricity of bis-tridentate Fe complexes (**40** and **41**, Figure 14), although the increased ligand flexibility results in faster deactivation of ES and shorter lifetimes.[63] Introducing an sp^3-hybridised carbon breaks the

conjugation and increases the flexibility of the ligand, while also increasing the distance between NHC units and allowing wider bite angles upon coordination to a metal.

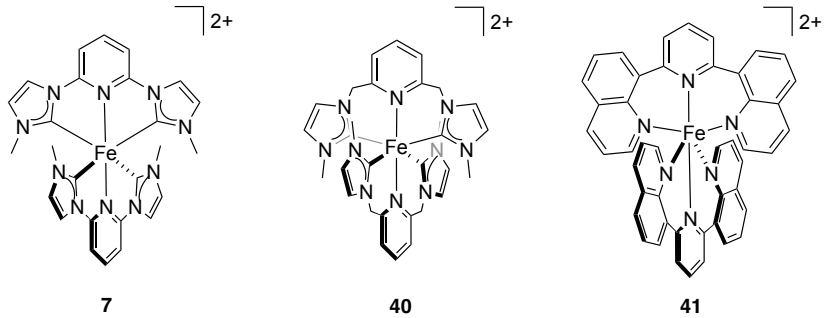

Figure 14 Molecular structures of complexes **40** and **41** that Darari reported as analogs of distorted octahedral complex **7**, in an attempt to improve octahedricity and ligand field splitting to extend the ES lifetimes.[63]

In this chapter, the syntheses of homoleptic complex **37** and heteroleptic complex **38** (Figure 15) are described. Both feature NHC-ligand **39** and their geometry and properties are analyzed and compared to complexes **11** and **14**, analogs differing only in the NHC-ligands design.

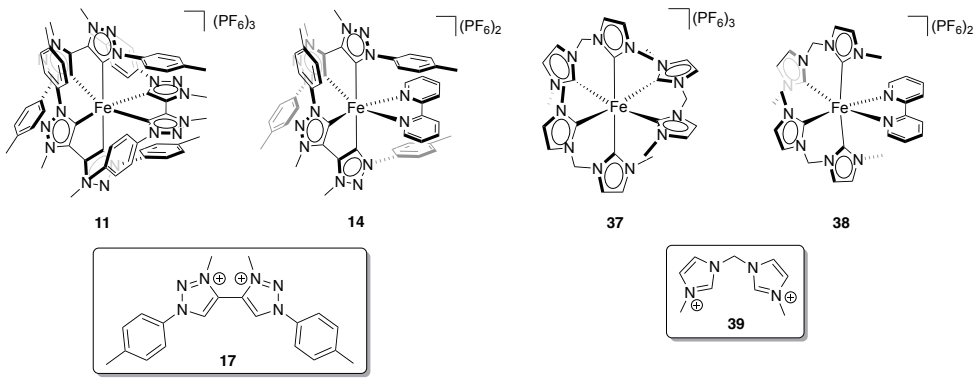

Figure 15 Molecular structures of previously published complexes **11**[27] and **14**[25] along with complexes **37** and **38**, reported in Paper I.

3.2 Synthesis, Structure and Geometry

Homoleptic complex **37** was synthesized by generating free carbene from ligand **39** in THF at - 78 °C, using a strong base (*t*-BuOK), before a THF solution of $FeBr_2$

was added. To obtain heteroleptic complex **38**, a stepwise process including previously discussed high-spin complex **16** was employed (Scheme 4).

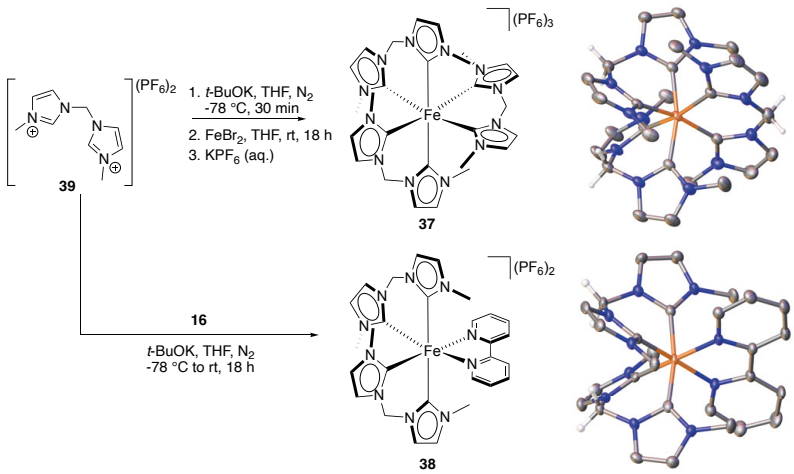

Scheme 4 Syntheses and crystal structures of complexes **37** and **38**. Gray: C atom; Orange: Fe atom; Blue: N atom. Hydrogen atoms, counter-anions, and co-crystallizing solvents are omitted for clarity (hydrogen atoms on the methylene bridges are shown).

Crystal structures obtained through single-crystal X-ray diffraction (SC-XRD) show the geometrical changes of **37** and **38** compared to **11** and **14**.[25, 27] The trans C-Fe-C bond angles of complexes **37** and **38** are further away from 180° than for the published complexes which indicates less octahedral structure (Entries 1-2 in Table 1).

Table 1 Bond angles (L-Fe-L) of **37** and **38** compared to previously reported **11** and **14**, respectively. n.a. = not applicable.

Complex	**11**[27]	**37**	**14**[25]	**38**
C–Fe–C (trans) (°)	179.0	166.2-166.8	172.6	169.7
C–Fe–N (trans) (°)	n.a.	n.a.	172.7-178.1	170.6-172.0
C–Fe–C (cis) (°) intraligand (bite angle)	79.2	85.4-89.5	79.3-80.0	85.5-85.9
N–Fe–N (°)	n.a.	n.a.	80.45	79.57
C–Fe–C (cis) (°) interligand	80.7-100.0	82.4-107.6	87.0-96.5	86.5-91.5
C–Fe–N (cis) (°)	n.a.	n.a.	85.8-101.0	86.6-100.8

However, as anticipated, the more flexible and extended ligand structure allows for wider bite angles, closer to the ideal 90° (Entries 3-4, Table 1). The NHC ligands **39** are non-planar when coordinated to Fe (dihedral angles 50.23-50.27° and 46.44-49.99° for **37** and **38**, respectively), apart from a single ligand on **37**, which is close to planar (dihedral angle 4.61°), similar to the bpy ligand on **38**, making the overall geometry of the two complexes similar. The geometries can be evaluated and directly compared using octahedricity (O) and planarity (P) factors,[64-66] calculated as root-mean-square error (RMSE) from ideal L-Fe-L bond angles and dihedral angles between the two cycles of each ligand, respectively (Table 2).

Table 2 Calculated geometrical values, octahedricity (O) and planarity (P), for **11**, **37**, **14** and **38**. Calculated through root-mean-square error (RMSE) from ideal L-Fe-L bond angles (O_{cis} – 90°, O_{trans} – 180°) and dihedral angles between the two cycles of each, ideally planar ligand, respectively.

	11[27]	**37**	**14**[25]	**38**
O_{cis}	9.61	8.32	7.13	6.11
O_{trans}	0.95	13.4	6.09	9.28
O_{total}	8.61	9.56	6.93	6.86
P	3.23	41.1	5.80	39.6

If the ligand sphere is octahedral, all L-Fe-L angles are 90°, or 180° for cis and trans positioned ligands, respectively, and O = 0. Similarly, flat ligands would exhibit dihedral angles of 0° and P = 0. By accommodating extended bite angles, ligand **39** reduces the deviation of the cis L-Fe-L angles from 90° in their complexes, resulting in a lower O_{cis} value than for complexes **11** and **14** (Table 2). However, the deviation of trans L-Fe-L angles from 180° (O_{trans}) is significantly larger for both **37** and **38**, compared to their counterparts **11** and **14** (Table 2). The overall octahedricity (O_{total}, Table 2), when all 15 L-Fe-L angles are given the same weight, is lower (higher O) for **37** than for **11**, while the degree of octahedricity (O_{total}) for **38** and **14** is comparable. The planarity of the ligands in **37** and **38** is lower (higher P, Table 2) than in **11** and **14**. This is not surprising given that ligand **39** has an sp^3 hybridized carbon between the NHC units, which ligand **17** does not, making the planar ligand structure less favorable. Interestingly, in homoleptic **37**, the NHC ligand with the bite angle closest to 90° is pseudo-planar, while the remaining two NHC ligands are twisted out of the plane and the bite angle is consequentially smaller. This observation can be explained with steric congestion around the metal center, where the non-planarity of **39** cannot be accommodated for all three ligands simultaneously and one is forced into a pseudo-plane. Since the bpy ligand in **38** does not feature an sp^3-hybridized carbon and is planar, the non-planarity of the two NHC ligands can be accommodated.

All in all, the increased ligand size and flexibility of ligand **39** compared to ligand **17** did not result in total geometry closer to the ideal octahedral geometry, despite significant geometry changes of complexes **37** and **38** compared to complexes **11**

and **14**. The ES dynamics of **37** and **38** (Figure 16) revealed that structural configurations and CT ES properties are related. The more flexible coordination sphere around the metal centre led to faster deactivation of the CT states and contributed to excited state lifetimes of 57.3 ps (^{2}LMCT) for **37** and 7.6 ps (^{3}MLCT) for **38**, compared to 100 ps (^{2}LMCT) for **11**[27] and 13 ps (^{3}MLCT) for **14**[25] (Table 3).

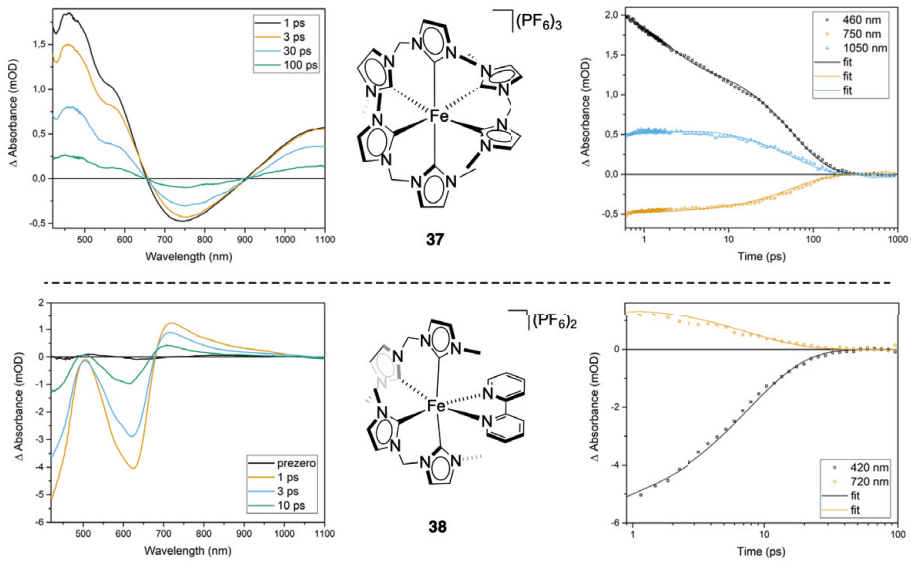

Figure 16 Top left: Transient absorption spectra of **37** (λ_{ex} = 400 nm). Top right: Transient absorption kinetics of **37** at indicated wavelengths. Bottom left: Transient absorption spectra of **38** (λ_{ex} = 620 nm). Bottom right: Transient absorption kinetics of **38** at indicated wavelengths. All measurements were carried out in dry and deaerated acetonitrile. The open symbols represent experimental data; solid lines are fits.

Time-dependent density functional theory (TD-DFT) calculations on the ^{3}MLCT state of **38** indicate a downhill deactivation pathway, through an MC state with a small energy barrier of ~0.04 eV (Figure 17, left). This can explain the shorter ES lifetimes of **38** compared to **14**. Unreliable computational characterization of the open-shell ^{2}LMCT state of **37** prohibited similar insights into the photophysics of the Fe(III) complex.

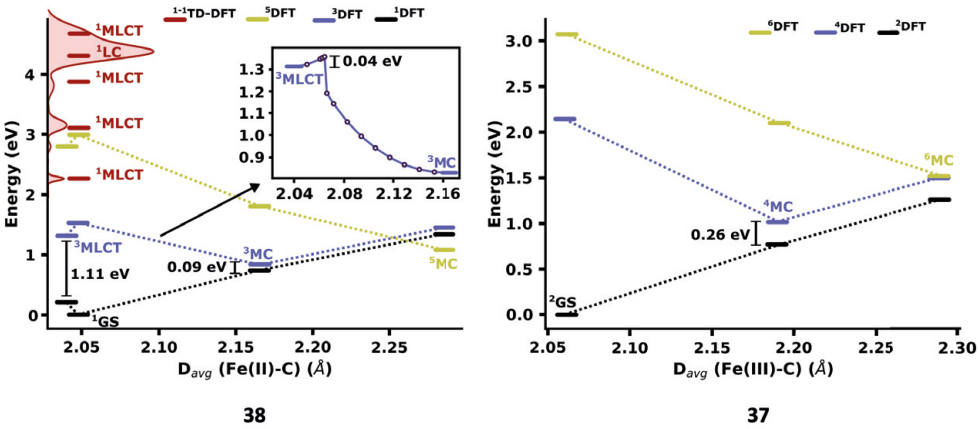

Figure 17 Left: DFT state energy diagram for **38** showing the lowest singlet, triplet and quintet states, together with the most intense singlet-singlet TD-DFT vertical excitations together with the fitted absorption spectra shown on the left axis. Right: DFT state energy diagram for **37** showing the lowest doublet, quartet, and hextet states. The Fe-L distances are calculated as the average for the six Fe-L bonds. All calculations were performed at the B3LYP*/6-311G(d) level in a polarizable continuum model (PCM) for acetonitrile.

Despite its shortened ES lifetime compared to **11**, **37** exhibits photoluminescence at room temperature, with a determined quantum yield (Φ_e) of 0.012% (compared to 0.03% for **11**[27], Table 3).

Table 3 Comparison of the selected photophysical properties of **11**[27], **37**, **14**[25] and **38**. All measurements carried out in deaerated acetonitrile.

Complex	**11**[27]	**37**	**14**[25]	**38**
ES	^{2}LMCT	^{2}LMCT	^{3}MLCT	^{3}MLCT
Absorption, λ_{max} (nm)	384, 528, 558	254, 420, 502	300, 432, 609	304, 410, 616
Extinction coefficient, ε ($M^{-1}cm^{-1}$)	1500 (528 nm)	2540 (502 nm)	3260 (609 nm)	5410 (616 nm)
ES lifetime, τ (ps)	100	57	13	7.6
Photoluminescence, λ_{em} (nm)	600	686	NA	NA
Quantum yield, Φ_e (in CH_3CN)	$(3 \pm 0.5) \times 10^{-4}$	$(1.2 \pm 0.1) \times 10^{-4}$	NA	NA

Conclusion

To investigate the effect of ligand rigidity and conjugation on metal complex properties, homoleptic Fe(III) complex **37** and heteroleptic Fe(II) complex **38** were synthesized and compared to previously reported complexes **11** and **14**.[25, 27] In both complexes, MIC-ligand **17** was replaced with NHC-ligand **39**, where the two carbene moieties are separated by an sp^3-hybridized methylene bridge.

In both complexes **37** and **38**, the bite angle of ligand **39** was larger and closer to the ideal 90° expected for octahedral coordination, while the degree of planarity of the ligands was lower. The geometric changes were evaluated through octahedricity (O) and planarity (P) factors. The overall octahedricity (O_{total}) of complex **38** (6.86) was found to be comparable to previously reported **14** (6.93), while slightly worse in the case of **37** (9.56) compared to previously reported **11** (8.61).

Instead of improving the octahedricity and photophysical properties, the more flexible coordination sphere around the metal center led to faster deactivation of the CT states, with ES lifetimes of 57.3 ps (^{2}LMCT) for **37** and 7.6 ps (^{3}MLCT) for **38**. Comparatively, these lifetimes are shorter, approximately halved, than for previously reported **11** (100 ps, ^{2}LMCT) and **14** (13 ps, ^{3}MLCT).

Our findings indicate that higher flexibility in the coordination sphere does not necessarily translate to improved geometrical or photophysical properties of Fe-NHC complexes. While the overall geometry changes and bite angles are increased, octahedricity of **37** and **38** is similar or worse than in the case of **11** and **14**.

4 Design, synthesis and characterization of a family of heteroleptic Fe-NHC complexes (Papers II and III)

4.1 Background

The synthesis and properties of heteroleptic Fe(II) complex **14** have been touched upon in preceding chapters. The stepwise synthesis employed to obtain the correct ligand stoichiometry separates it from the majority of Fe-NHC complex syntheses, while the coordination of different ligand types introduces potential directionality of electron movement upon excitation.[46] With four NHC units donating electron density to the metal centre, the ^{3}MLCT ES lifetime of **14** (13 ps) was increased by two orders of magnitude compared to **2** with no NHC ligand (130 fs).[25] If all ligands in the coordination sphere of Fe are NHCs, oxidation of the Fe(II) metal is promoted and the stable oxidation state of the complex tends to shift to Fe(III).[27-28] This influences the ES dynamics of the complex and changes the CT states from MLCT to LMCT. Potential applications for the complexes are also different since redox potentials have shifted.

In this chapter the synthesis, isolation and characterization of **14** in two oxidation states is described. The same is done for three derivatives of **14**, with functionalized bpy groups, and their properties discussed and compared to understand their structure-property relationships.

4.2 Synthesis

4.2.1 Synthesis of heteroleptic derivatives of 14

Starting from complex **14**, different synthetic strategies aimed at introducing anchoring groups (-COOH) on the bpy ligand have been explored. In addition to the

option to investigate the performance in PV applications, the acid groups are electron withdrawing and will influence the electronic properties of the complex. An obvious starting point was to attempt the published synthesis of **14**[25] with commercially available 2,2'-bipyridine-4,4'-dicarboxylic acid (**40**) instead of unsubstituted bpy ligand **15**. Similar to the main problem in Chapter 2, the poor solubility of **40** in EtOH was the main reason for the unsuccessful reaction with $FeCl_2$. The same applies for alkyl ester derivatives **41-43** of ligand **15** (Scheme 5).

The synthesis of [Fe(btz)$_2$(2,2'-Bipyridine-4,4'-dicarboxylic acid)](PF$_6$)$_2$ (**46**) starting from bpy ligands with carboxylate functionality is in place prior to complexation (**40**-**43**) did not prove successful. The alternative strategy of altering the functionality of **15** (or its derivatives) already coordinated to a metal was investigated. Initial attempts revolved around coordinating halogen-substituted ligands **44** or **45** to $FeCl_2$, where the halogens could then be transformed into a variety of functional groups. **44** and **45** exhibit higher solubility in EtOH than **40-43** and precipitates were obtained for both after reactions with $FeCl_2$. However, when the second step of the syntheses, where carbene ligands **17** are introduced were attempted, the desired heteroleptic complexes could not be detected. The reaction crude mainly contained halogenated derivatives of **2**, most likely from the initial reaction of **44** and **45** with $FeCl_2$.

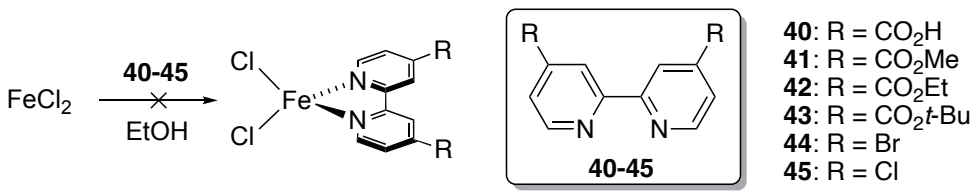

Scheme 5 Unsuccessful attempts at the first step in the synthesis of **46**.

Functional group alteration by utilising redox chemistry was investigated as well. 4,4-Dimethyl-2,2'-bipyridine (**47**) is commercially available and dissolves when heated to 60 °C in EtOH. Reaction of ligand **47** with $FeCl_2$ in EtOH (Scheme 6) resulted in the formation of intermediate [$FeCl_2$(4,4-Dimethyl-2,2'-bipyridine)] (**48**) as a red-orange precipitate which was collected through filtration. It should be noted that the reaction was significantly slower (5 h) than the previously reported synthesis of unsubstituted analog **16** (5 min). The second reaction step where **17** was coordinated proved successful as well, yielding **49** as a black solid (dark green in dilute solution) (Scheme 6). Unfortunately, attempts to oxidize the methyl groups of **49** to carboxylic acid groups with $KMnO_4$ to obtain **46** were not successful and **49** was recovered (Scheme 6).

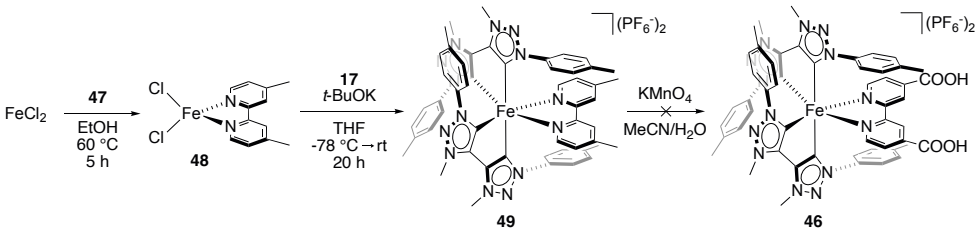

Scheme 6 The two-step synthesis of **49** from $FeCl_2$ and unsuccessful attempt to obtain **46** through $KMnO_4$ oxidation from **49**.

In 2015, Duchanois reported the synthesis of an Fe-NHC complex with carboxylic acid groups on the pyridyl ligands by $KMnO_4$ oxidation of a precursor complex containing 2-furanyl-substituted ligands.[67] To make use of that strategy, the synthesis of 4,4'-di(furan-2-yl)-2,2'-bipyridine (**50**) was developed (Scheme 7). The Suzuki-Miyaura coupling can effectively couple sp^2-hybridized carbons using a Pd(0) catalyst under alkaline conditions.[68-70] The method has gained a lot of attention and is under constant development to allow for more efficient reactions on less reactive substrates. Bpy ligand **44** and 2-furanylboronic acid (**51**) are both commercially available starting materials well suited for coupling reactions. The Suzuki-Miyaura coupling presented in Scheme 7 yielded ligand **50** as a waxy off-white solid.

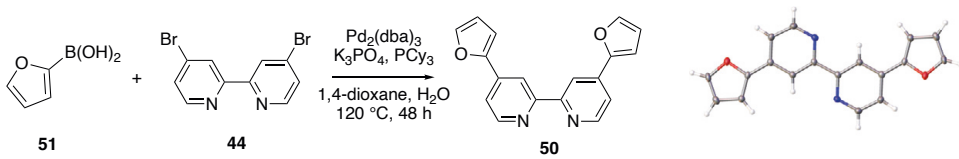

Scheme 7 The synthesis of **50** through Suzuki-Miyaura coupling of **51** and **44**, along with the crystal structure of **50**. Gray: C atom; Red: O atom; Blue: N atom.

The solubility of **50** in EtOH is poor, even at 60 °C. However, when added as a suspension to an EtOH solution of $FeCl_2$ at the same temperature, intermediate complex **52** was obtained as a red precipitate after 16 h reaction time (Scheme 8). When dissolved in THF with ligand **17** and *t*-BuOK base, complex **53** was obtained as a black solid (green in dilute solution) (Scheme 8). Finally, the oxidative cleavage of the furanyl groups by $KMnO_4$ was performed, following a procedure adapted from the aforementioned reference.[67] After filtration of the reaction mixture, a solution containing **46** was obtained. Isolation from the crude reaction mixture proved challenging, as the increased polarity and H-bonding of the COOH groups affected the solubility of the complex.

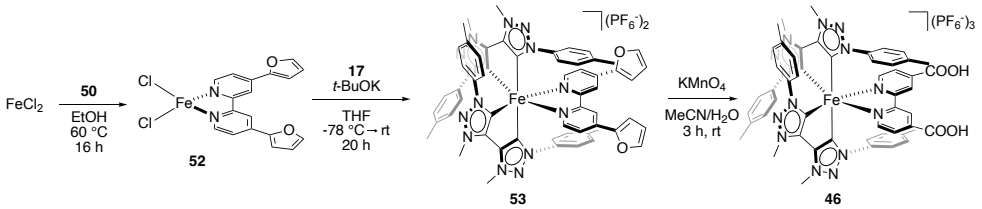

Scheme 8 The synthesis of **46** from $FeCl_2$, through oxidative cleavage by $KMnO_4$ of the 2-furanyl groups of **53**.

4.2.2 Oxidation states Fe(II) and Fe(III)

In addition to challenges arising from the presence of two carboxylic acid groups, the formal oxidation state of the complex also became a complication. Until the permanganate oxidation of **53**, **14** and its derivatives (**49** and **53**) had been synthesized and isolated in the formal Fe(II) oxidation state (18 e^-, d^6). Surprisingly, this was not the case for crude **46**. ^{1}H NMR analysis gave resonances with paramagnetic shifts, indicating the presence of Fe(III), and after attempted purification there were strong indications that both Fe(II) (**46**$^{2+}$) and Fe(III) (**46**$^{3+}$) complexes were present. Attempts to obtain **46**$^{2+}$, purely as Fe(II), through dithionite ($Na_2S_2O_4$) reduction were eventually successful (Scheme 9). However, **46**$^{2+}$ can be oxidized to **46**$^{3+}$ by O_2 and even in the solid state under inert atmosphere, **46**$^{2+}$ is short-lived. This is surprising from an organometallic perspective since the electron counting of the Fe(III) complex gives 17 e^-, d^5.

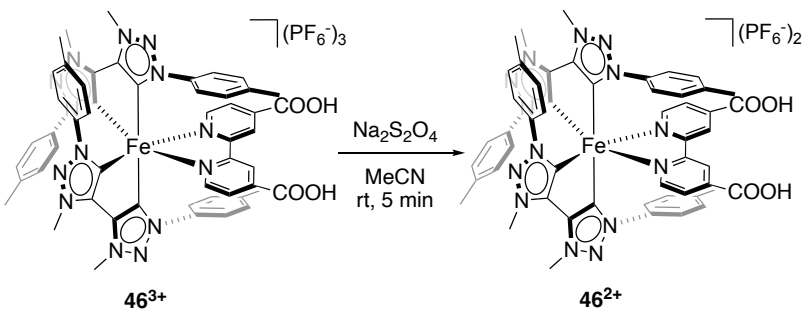

Scheme 9 Reduction of Fe(III) **46**$^{3+}$ to Fe(II) **46**$^{2+}$ by sodium dithionite ($Na_2S_2O_4$).

Given the instability of **46**$^{2+}$, isolation of **46** in a single oxidation state is more convenient as **46**$^{3+}$, since spontaneous reduction to Fe(II) or oxidation to Fe(IV) is unlikely.

During the purification of a batch of **49**$^{2+}$ on a Bio-Bead S-X1 size-exclusion column, an unexpected color change from dark green to red was observed when the substance reached the later part of the column. The color change was later explained by oxidation of the Fe(II) complex **49**$^{2+}$ to Fe(III) **49**$^{3+}$ by atmospheric oxygen, likely

induced by the presence of trace amounts of dilute acetic acid used to clean the column prior to use. Following this discovery, a procedure was developed where HPF_6 was used to oxidize $\mathbf{14}^{2+}$, $\mathbf{49}^{2+}$, $\mathbf{53}^{2+}$ and $\mathbf{46}^{2+}$ from Fe(II) to Fe(III) (Scheme 10). This specific acid was chosen to make sure that there was an excess of PF_6^- present in solution to accommodate the additional positive charge acquired after the Fe(II) to Fe(III) oxidation.

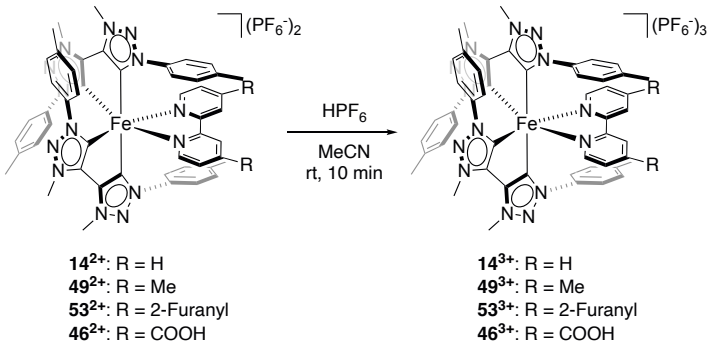

Scheme 10 Oxidation of Fe(II) $\mathbf{14}^{2+}$, $\mathbf{49}^{2+}$, $\mathbf{53}^{2+}$ and $\mathbf{46}^{2+}$ to Fe(III) $\mathbf{14}^{3+}$, $\mathbf{49}^{3+}$, $\mathbf{53}^{3+}$ and $\mathbf{46}^{3+}$ by atmospheric O_2, induced (if not spontaneous) by lowered pH.

After isolation and purification through a combination of techniques, including alumina column chromatography, size-exclusion column chromatography, precipitation from solution with antisolvent and crystallization, identity and purity of complexes $\mathbf{14}^{3+}$, $\mathbf{49}^{2+}$, $\mathbf{49}^{3+}$, $\mathbf{53}^{2+}$, $\mathbf{53}^{3+}$, $\mathbf{46}^{2+}$ and $\mathbf{46}^{3+}$ has been confirmed with NMR spectroscopy, HR-MS, CHN elemental analysis and SC-XRD (Details in Paper II and III and corresponding Supporting Information).

4.3 Ground-state characterization

4.3.1 Crystal structures and geometries

The crystal structures of $\mathbf{14}^{3+}$, $\mathbf{49}^{2+}$, $\mathbf{49}^{3+}$, $\mathbf{53}^{2+}$, $\mathbf{53}^{3+}$, $\mathbf{46}^{2+}$ and $\mathbf{46}^{3+}$ have been obtained by SC-XRD (Figure 18). For the complexes that are stable in air (all but $\mathbf{46}^{2+}$), crystals were grown by slow diffusion of diethyl ether into an acetonitrile solution of the respective complex. Especially challenging were $\mathbf{49}^{2+}$ and $\mathbf{53}^{2+}$, which had a tendency to form microcrystalline materials, unfit for diffraction analysis. Ultimately, single crystals were obtained by placing the crystallization chambers in the freezer at -18 °C.

The COOH-bearing complexes **46**$^{2+}$ and **46**$^{3+}$ run the risk of being deprotonated by trace water present in the solvent and were therefore crystallized from dry, degassed solvents. The complexes additionally share the ability to form H-bonded dimers and precipitate out of solution. This ability is enhanced without water present and at higher concentrations, which are unfortunately conditions where crystal growth is promoted. **46**$^{2+}$ is furthermore unstable as Fe(II), especially in solution and was therefore crystallized following a different procedure. Pre-dried glassware (test-tube and vial) were used and the anhydrous solvents were carefully deaerated with argon prior to use. After sealing the vial containing the setup, it was placed in an even larger container, filled with argon. Eventually, single crystals were obtained, which were immersed in oil for SC-XRD mounting directly after opening the system.

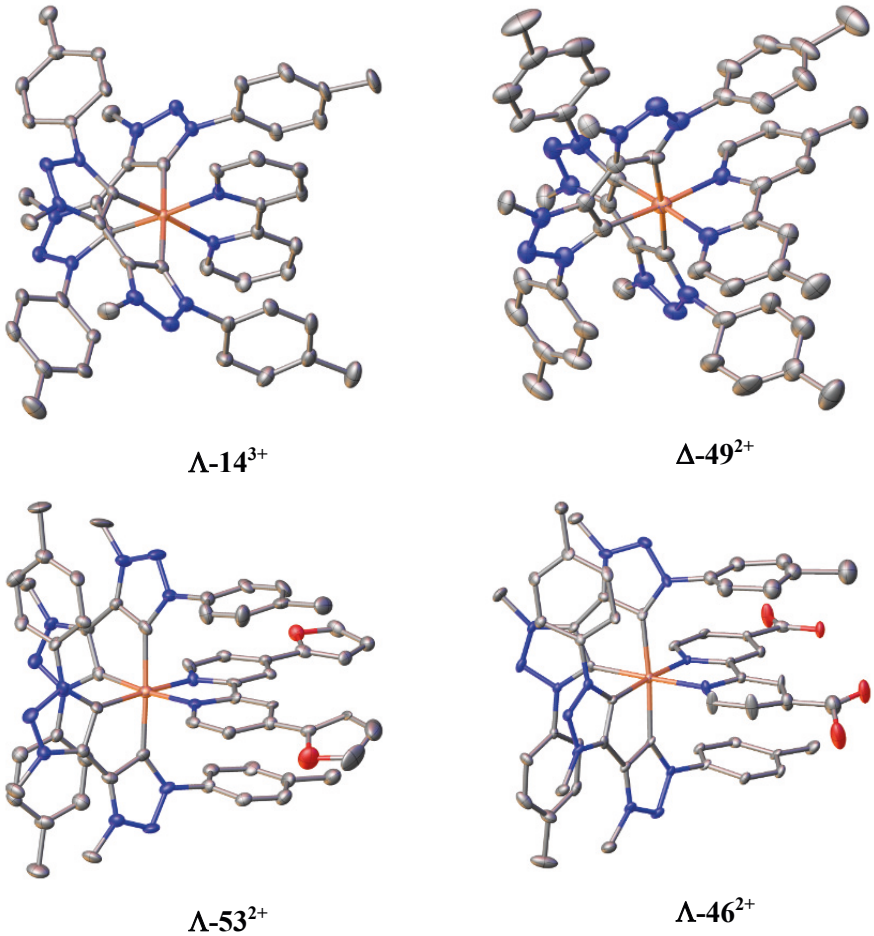

Figure 18 Crystal structures of complexes **Λ-14**$^{3+}$ (top left), **Δ-49**$^{2+}$(top right), **Λ-53**$^{2+}$ (bottom left) and **Λ-46**$^{2+}$ (bottom right). Gray: C atom; Red: O atom; Orange: Fe atom; Blue: N atom. Hydrogen atoms, counter-anions, and co-crystallizing solvents are omitted for clarity.

The resolved crystal structures of the complexes all show the same octahedral environment around Fe, with minor changes in bond length and bond angles, for the most part independent of the oxidation state of iron and the substitution on bipyridine. The ligand orientation is governed by interligand π-π stacking, where one tolyl group of each **17** ligand is placed above or under the bipyridine rings, with a small displacement. Additionally, there are π-π interaction between the other tolyl groups and a triazole on alternative btz ligand. As expected, for racemic mixtures of two enantiomers (Λ or Δ), the crystal structures obtained were found to contain both enantiomers.

During computational structural optimization of $\mathbf{14}^{2+}$ and $\mathbf{49}^{2+}$ using the crystal structure coordinates as starting points, two structural conformers were identified as low energy conformers for each complex. The structural differences between them are small, with the main changes occurring at the tolyl groups of **17** pointing away from the bipyridine ligand. Having at least two structural minima close in energy has large implications for NMR spectroscopy of these complexes, as will be discussed in the next section.

Similar to **37** and **38**, discussed in Chapter 3, the geometries of all complexes discussed in this chapter were further analyzed using the octahedricity factor (Table 4).[64-66] The trends that can be observed from the octahedricity factor are that by comparing the Fe(II) and Fe(III) oxidation states of each complex, the Fe(II) state is more octahedral than Fe(III) for **14**, **49** and **53**, while the opposite is true in the case of **46**. The O_{trans} is lower for Fe(III) than Fe(II) for all complexes except $\mathbf{53}^{3+}$, which has higher O_{trans} than most of the Fe(II) complexes and contributes to the lowest degree of octahedricity in this set of complexes. The complex closest to the ideal octahedral geometry is the previously published parent complex, $\mathbf{14}^{2+}$.

Table 4 Calculated octahedricity (O) values for both oxidation states of **11**, **37**, **14** and **38**. Calculated through root-mean-square error (RMSE) of L-Fe-L angles, obtained from crystallographic data, from ideal L-Fe-L bond angles (O_{cis} – 90°, O_{trans} – 180°).

	$\mathbf{14}^{2+}$ [25]	$\mathbf{14}^{3+}$	$\mathbf{49}^{2+}$	$\mathbf{49}^{3+}$	$\mathbf{53}^{2+}$	$\mathbf{53}^{3+}$	$\mathbf{46}^{2+}$	$\mathbf{46}^{3+}$
O_{cis}	7.13	8.79	7.88	8.83	8.28	8.94	8.82	8.59
O_{trans}	6.09	3.84	5.16	3.28	4.51	5.48	4.37	3.96
O_{total}	6.93	8.05	7.42	8.03	7.67	8.36	8.13	7.88

4.3.2 NMR spectroscopy

All Fe(III) complexes ($\mathbf{14}^{3+}$, $\mathbf{49}^{3+}$, $\mathbf{53}^{3+}$ and $\mathbf{46}^{3+}$) have a low-spin, d^5 electron configuration, as confirmed by electron paramagnetic resonance (EPR) and magnetization measurements. As paramagnetic species, their ^{1}H NMR spectra expectedly show broad, paramagnetically shifted resonances and ^{13}C NMR signals were not observed.

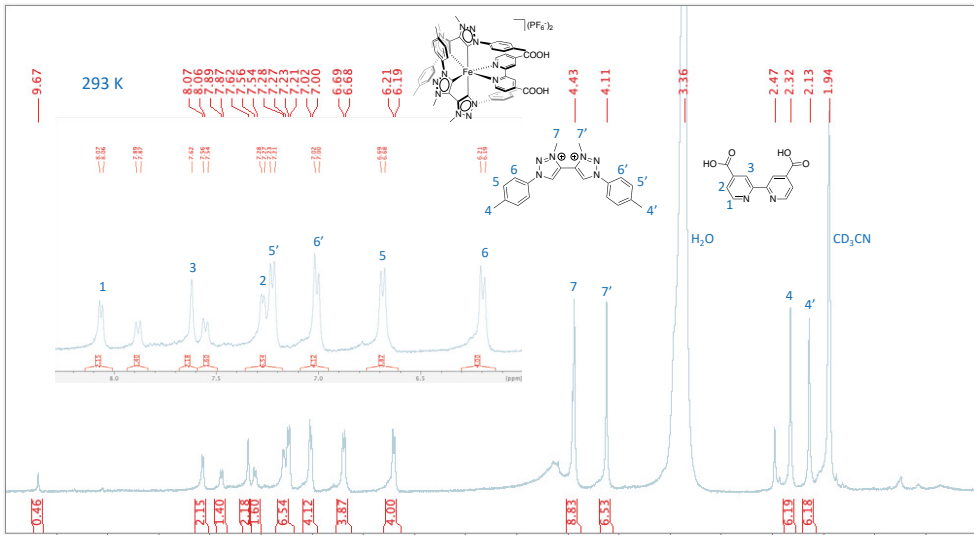

Figure 19 Assigned ^{1}H NMR spectrum of **46**$^{2+}$ (2.0 mg in 0.4 mL MeCN-d_3, $Na_2S_2O_4$ and 1 drop of D_2O added to ensure Fe(II)) at r.t. (293 K).

On the other hand, the diamagnetic low-spin, d^6, Fe(II) complexes were expected to give well resolved ^{1}H and ^{13}C NMR signals. This, however, was only the case for **46**$^{2+}$ (Figure 19). At room temperature, ^{1}H NMR spectra of the other Fe(II) complexes (**14**$^{2+}$, **49**$^{2+}$ and **53**$^{2+}$) showed fewer and broader resonances than anticipated. When cooled down, the signals became narrower and the chemical shift of some resonances changed (Figure 20). This indicates a dynamic system, where the exchange is slowed down at lower temperatures. In acetone-d_6, which was used instead of more commonly used MeCN-d_3 due to its lower freezing point, the best resolution of **14**$^{2+}$ was obtained at -75.6 °C (calibrated with pure MeOH), although still with some dynamic parts (Figure 20). Cooling it even further did not improve the results, since the temperature was approaching the freezing point of acetone (- 94 °C)[71]. Two-dimensional spectra (COSY, HSQC and HMBC) recorded at - 75.6 °C were analyzed to assign the ^{1}H NMR spectrum of **14**$^{2+}$ (Figure 21).

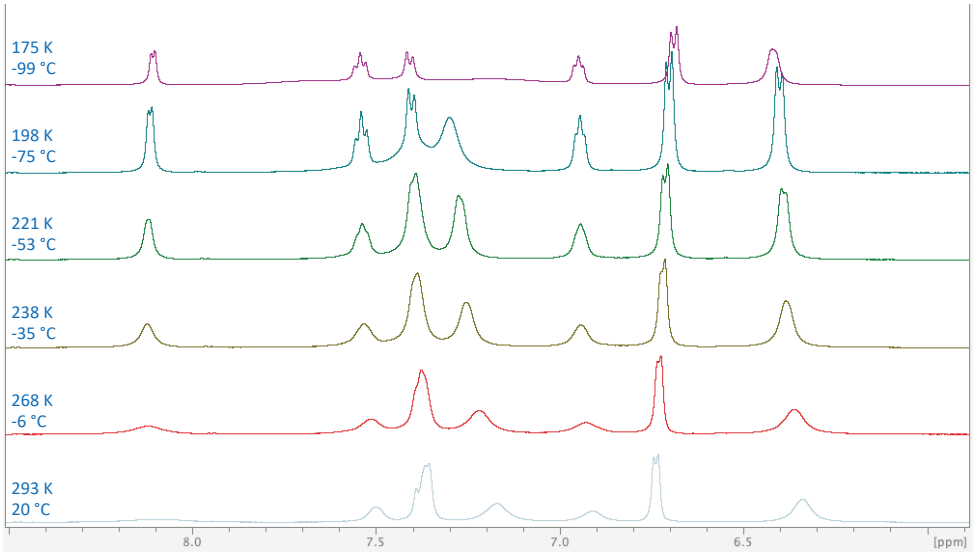

Figure 20 Spectral changes in the aromatic region (δ = 8.5 – 6.0 ppm) of ^{1}H NMR of **14**$^{2+}$ with varying temperatures. Data obtained on a 500 MHz NMR spectrometer. Temperature calibrated with pure MeOH as NMR thermometer.

Four resonances are expected from the protons located on the bipyridine ligand of **14**$^{2+}$, as is found (H1-H4, Figure 21). Compared to the reported chemical shifts of $[Fe(bpy)_3]^{2+}$ **2**,[72] all bipyridine resonances in **14**$^{2+}$ are significantly shielded by up to 370 Hz. This can be explained by the parallel-displaced π-π stacking between the bipyridine ligand and one tolyl group from each **17** ligand, which can be observed in the crystal structure of the complex. One of the shielded bipyridine signals (H4) originates from protons pointing away from the centre of the magnetic field induced by the tolyl π-system. This results in significantly smaller shielding effect (~170 Hz), compared to the shielding of the other three resonances (H1-H3).

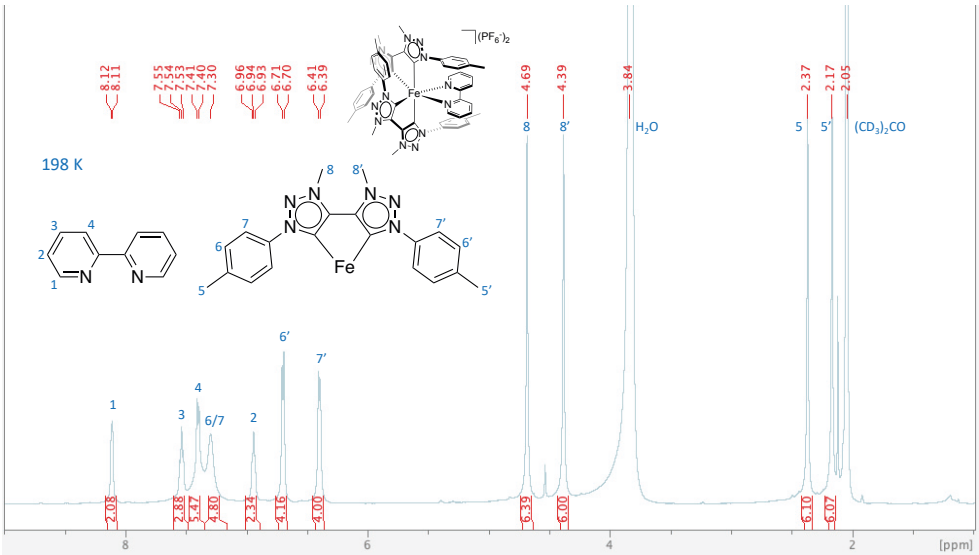

Figure 21 Assigned ^{1}H NMR spectrum of **14**$^{2+}$ in acetone-d_6 at -75.6 °C (198 K), measured on a 500 MHz NMR spectrometer. Temperature calibrated with pure MeOH as NMR thermometer.

For the two **17** ligands, the picture is more complex. By looking at the number of protons and their distribution on the two ligands, one might expect two singlets, originating from the two sets of CH_3 groups, and two sets of aromatic doublets, originating from the tolyl groups. This is not the case, as due to the symmetry induced when the ligands are coordinated to a metal, the number of signals is doubled. As can be seen from the crystal structure (Figure 22), one tolyl group of a **17** ligand (H6'-H7') is located close to the bipyridine ligand, while the other tolyl group of the same ligand is on the opposite site of the metal (H6-H7) with non-equivalent chemical environment. Because of the pseudo-C_2 symmetry through Fe in the Fe-bpy plane, the other **17** ligand is chemically equivalent and therefore the signals are not split further. The magnetic anisotropy mentioned before that affects the chemical shift of the π-π stacking aromatic rings can explain the large difference in chemical shift between the tolyl group resonances within each of the **17** ligands. The tolyl protons above or under the bipyridine ligand (H6'-H7') are more shielded than protons on the other tolyl group (H6-H7), the resonance originating from H6 overlaps with H4.

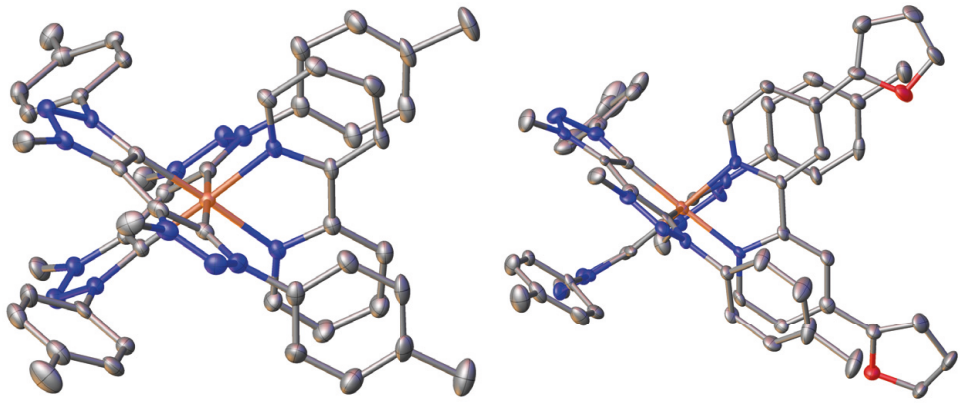

Λ-14^{3+} **Λ-53**$^{2+}$

Figure 22 Crystal structures of complexes **Λ-14**$^{3+}$ (left) and **Λ-53**$^{2+}$ (right), showing the π-π interactions between tolyl groups of ligands **17** with ligands **15** and **50**, respectively. Gray: C atom; Red: O atom; Orange: Fe atom; Blue: N atom. Hydrogen atoms, counter-anions, and co-crystallizing solvents are omitted for clarity.

Quantum chemical calculations of **14**$^{2+}$ predicted two structural minima of low energy. The structural differences are small, mostly involving the orientation of the tolyl groups that are not involved in the π-π stacking with bpy. This is in agreement with the assignment of the ^{1}H NMR (Figure 21) where the resonance that shows the smallest improvement (H6-H7) with reduced temperature (and is broadened into the baseline at -99 °C, Figure 20) is identified as these tolyl groups.

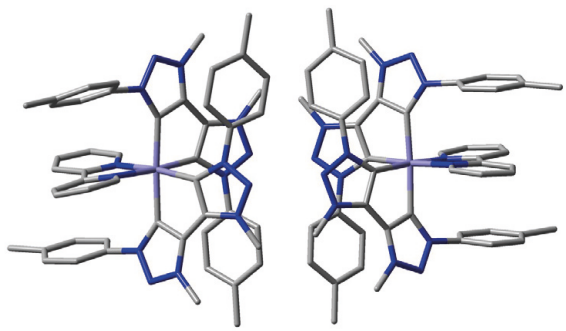

14^{2+}

Figure 23 Optimized structures of **14**$^{2+}$ showing two low-energy conformers obtained at B3LYP+D2/6-311G*, SDD(Fe) level of theory in CH_3CN.

4.3.3 Absorption spectroscopy and extinction coefficients

The absorption spectra of the Fe(II) complexes **14**$^{2+}$, **49**$^{2+}$, **53**$^{2+}$ and **46**$^{2+}$ all share the same features. A strong absorption that stretches into the UV region below 250 nm is followed by a signal at ~300 nm (Figure 24). In the visible region, two broad MLCT transitions are observed, the higher energy signal appearing between ~350 (**49**$^{2+}$) and 550 nm (**46**$^{2+}$). The lower energy signal has lower molar extinction than the other MLCT transition and is broader. In fact, it looks like it is made up of at least two transitions. The energy of those transitions also varies, starting from ~500 nm (maximum at ~600 nm) for **49**$^{2+}$, all the way to almost 800 nm (maximum at ~670 nm) for **46**$^{2+}$ (Figure 24). The energies of the MLCT transitions are related to the electron donating ability of the functional groups on bipyridine, where methyl groups are electron donating, increasing the electron density of the bipyridine on **49**$^{2+}$ compared to **14**$^{2+}$. This destabilises the π* orbital and, assuming that the molecular orbitals of the metal are mostly unaffected, this will result in higher energy transition. Similarly, EWGs such as COOH reduce the electron density on the bipyridine, which stabilises the π* orbitals and reduces the energy of the MLCT transitions.

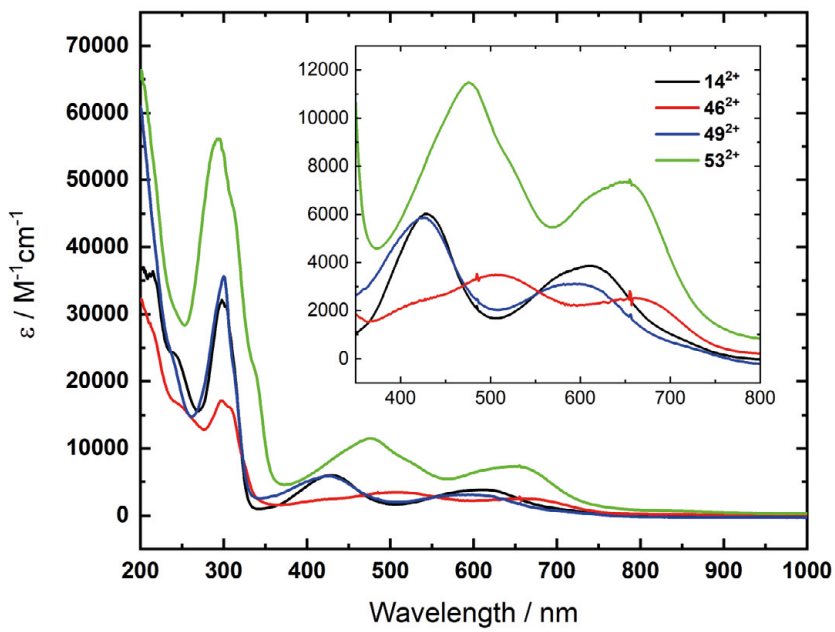

Figure 24 Absorption spectra of the Fe(II) complexes **14**$^{2+}$, **49**$^{2+}$, **53**$^{2+}$ and **46**$^{2+}$ obtained during spectroelectrochemistry measurements.

As discussed in the introduction, one of the LMCT transitions of d_5 Fe(III) complexes is from a ligand based π orbital into an half-filled, metal t_{2g} orbital. This is reflected in the absorption spectra of **14**$^{3+}$, **49**$^{3+}$, **53**$^{3+}$ and **46**$^{3+}$ (Figure 25), where the LMCT transitions observed in the visible region of the spectra are mostly unaffected by the functionality change on bipyridine. Following a large transition at ~300 nm there is a significantly smaller transition at ~400 nm and at least two overlapping transitions between ~500 and 650 nm.

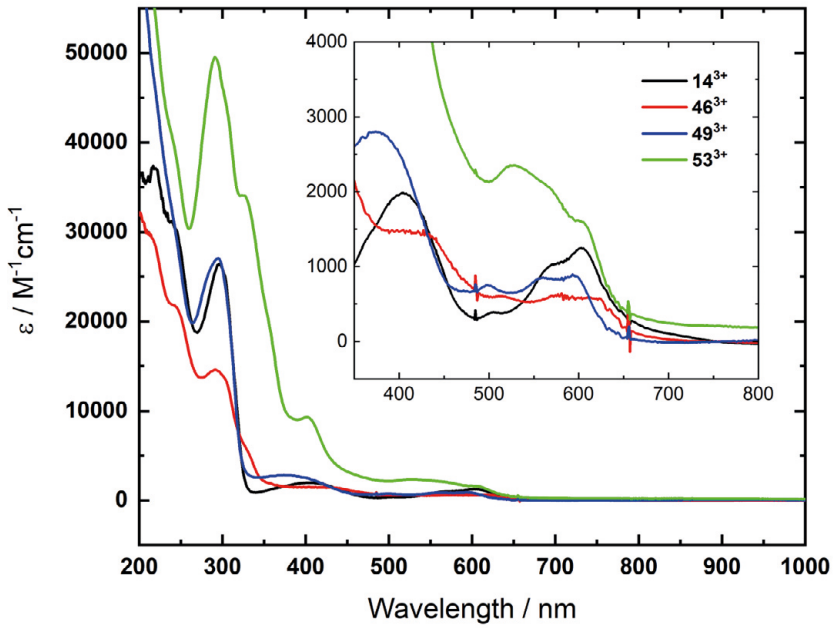

Figure 25 Absorption spectra of the Fe(III) complexes **14**$^{3+}$, **49**$^{3+}$, **53**$^{3+}$ and **46**$^{3+}$ obtained during spectroelectrochemistry measurements.

Complexes **53**$^{2+}$ and **53**$^{3+}$ stand out when compared to the other complexes sharing the same oxidation state in having noticeably the highest molar extinction coefficient (ε) (Figures 24 and 25, summarized in Table 5). In addition, complex **53**$^{3+}$ shows two features (shoulder at ~325 nm and broad transition at ~520 nm) that are not shared with the other Fe(III) complexes in Figure 25. Currently, the reason is unknown, but an interesting observation on **53**$^{3+}$ is that it was identified as the least octahedral (highest O_{total}, Table 4) out of the complexes investigated here. Especially the trans L-Fe-L angles were comparatively further away from ideal octahedral angles.

In their protonated form, the COOH groups of **46**$^{2+}$ (and **46**$^{3+}$) are electron withdrawing and give rise to a red-shift of the MLCT transitions, compared to the

other Fe(II) complexes in Figure 24. When deprotonated, the electronic properties of the acid groups change and they become less electron withdrawing, resulting in a blue-shift of the MLCT absorption by up to 50 nm. To ensure consistent data collection, all measurements were performed in anhydrous MeCN. The absorbance of $\mathbf{46}^{2+}$ was measured at different concentrations (88-1408 μM) in anhydrous MeCN to evaluate whether the small amount of water would affect the spectra (Figure 26).[46]

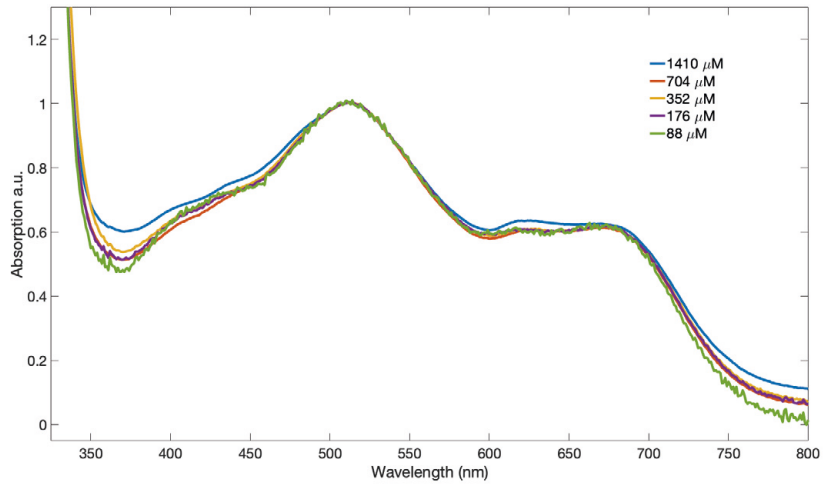

Figure 26 The absorption spectra of $\mathbf{46}^{2+}$ at different concentrations in anhydrous (16 ppm H_2O) MeCN. Spectra normalized at 509 nm.

The absorption was unchanged from at least 100-700 μM but above 1400 μM concentrations, slightly stronger absorption was found at 400-450 nm and around 620 nm, which is where $\mathbf{46}^{3+}$ transitions are strongest, indicating that oxidation has occurred despite efforts to prepare and measure samples under inert atmosphere. No sign of deprotonation was observed. The same experiment was also performed with $\mathbf{46}^{3+}$ (22-700 μM) and the results were similar, with no sign of deprotonation. The only spectral changes observed were for the lowest concentration (22 μM), where the measured absorption is close to the detection limit of the spectrometer.

$$\boldsymbol{A = \varepsilon \cdot C \cdot l} \qquad (1)$$

From the dilution series, the molar absorption coefficient (ε) of the complexes can be calculated, according to the Beer-Lambert law (equation 1), where A is the absorbance at a certain molar concentration (C) in a cuvette of path length l. The results are summarized in Table 5.

The energy shift following protonation/deprotonation of carboxylic acid groups of $\mathbf{46}^{2+}$ is observable by eye from the color shift in solution. The protonated form of

46^{2+} is purple, while the deprotonated form, along with **14**$^{2+}$, **49**$^{2+}$ and **53**$^{2+}$, is of strong green color, not to be confused with the different (brighter) shade of green that **46**$^{3+}$ can have. **14**$^{3+}$, **49**$^{3+}$, **53**$^{3+}$ and **46**$^{3+}$ all have different shades of red color when in the Fe(III) state. However, at least two of them have additional colors in solution and as crystals. **14**$^{3+}$ has a blue colour but from some angles (longer "path" length or layer thickness) it appears red or pink, while **46**$^{3+}$ appears green but through thicker layers has a red color (absorption spectrum shown in Figure 27). This phenomenon, where the hue (color) of a material, not only brightness and saturation, is dependent on the depth of the solution, is known as dichromatism. It is explained through physical chemistry properties of the dichromatic substance as well as the physiological response of the human visual system to color.[73] An example of dichromatic substance is pumpkin seed oil, which looks red in a bottle but when the layer of pumpkin seed oil is thinner than 0.7 mm, the oil appears green.[73] The physical property required for a substance to show dichromatism is that, in the visible region of its absorption spectrum, it has one wide and shallow local minimum and one narrow and deep local minimum (Figure 27). The width of the minima can be limited by the end of the visible range of the human eye. The perceived hue for thin layers is determined by the position of the wide, shallow minimum (green in Figure 27) in the visible region of the absorption spectrum, while the transmitted light at the deep, narrow minimum (red in Figure 27) begins to dominate when thickness increases. In thin layers, the broader transmission at the wide minimum outcompetes the higher transmission at the deep minimum, while in thicker layers, transmission at the shallow minimum is hampered and the deep minimum defines the perceived hue.

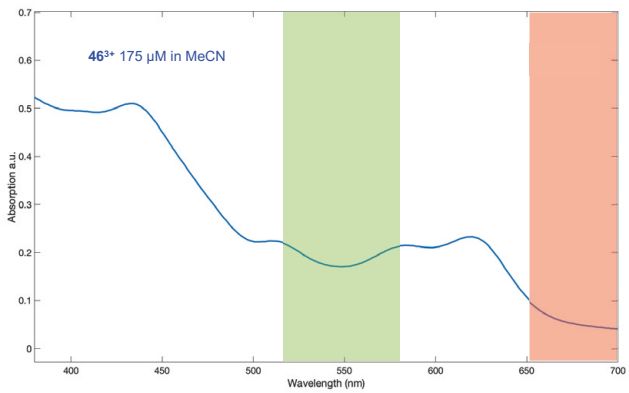

Figure 27 Absorption spectrum of **46**$^{3+}$ in the visible region of the electromagnetic spectrum with two absorption minima highlighted, explaining the dichromatic properties.

4.4 Photophysics, electrochemistry and magnetic properties

4.4.1 Transient absorption spectroscopy

The excited state dynamics of all complexes, in both Fe(II) and Fe(III) oxidation states were studied using time-resolved absorption spectroscopy. Complexes in the Fe(II) oxidation state (**49**$^{2+}$, **53**$^{2+}$ (Figure 28, top) and **46**$^{2+}$ (Figure 28, bottom)) all show excited state decay and ground state bleach recovery very similar to the unsubstituted, previously reported complex **14**$^{2+}$.

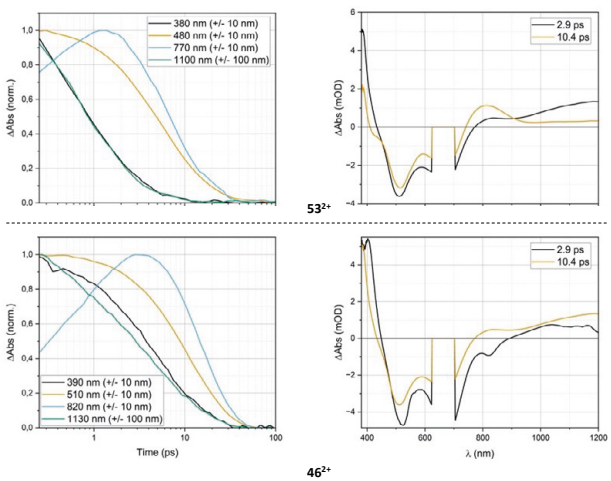

Figure 28 Transient absorption of **53**$^{2+}$ (top) and **46**$^{2+}$ (bottom) following 660 nm excitation. Left: Kinetics at selected wavelengths. Right: Species associated spectra (SAS) generated by a global fit, showing 2.9 ps and 10.4 ps decay components for both.

When it comes to the Fe(III) complexes, three of them show very similar features in transient absorption spectroscopy with ^{2}LMCT lifetime of ~18 ps. Only **53**$^{3+}$ is fractionally different, with shorter ES lifetime of ~13 ps.

That means that all four complexes discussed in this chapter, in both of their Fe(II) and Fe(III) oxidation states have ES lifetimes between 5-20 ps.

Table 5 Comparison of the selected photophysical properties of **14**$^{2+}$, **14**$^{3+}$, **49**$^{2+}$, **49**$^{3+}$, **53**$^{2+}$, **53**$^{3+}$, **46**$^{2+}$ and **46**$^{3+}$. All measurements carried out in deaerated acetonitrile. n.d. = not determined

Complex	Absorption, λ_{max} (nm)	Extinction coefficient ε ($M^{-1}cm^{-1}$)	ES	ES lifetime, τ (ps)	Photoluminescence λ_{em} (nm)
14^{2+}	300 432 609	29500 (300 nm) 5080 (432 nm) 3260 (609 nm)	^{3}MLCT	13	-
14^{3+}	389 567 602	n.d.	^{2}LMCT	18	n.d.
49^{2+}	427 572 601	n.d.	^{3}MLCT	6.4	-
49^{3+}	377 560 594	n.d.	^{2}LMCT	18	n.d.
53^{2+}	294 476 649	52700 (294 nm) 9200 (476 nm) 5800 (649 nm)	^{3}MLCT	10.4	-
53^{3+}	403 527 601	7670 (403 nm) 1890 (527 nm) 1270 (601 nm)	^{2}LMCT	12.7	650
46^{2+}	509 671	3680 (509 nm) 2290 (671 nm)	^{3}MLCT	10.4	-
46^{3+}	584 619	1280 (584 nm) 1380 (619 nm)	^{2}LMCT	18.7	670

4.4.2 Electrochemistry and Spectroelectrochemistry

Electrochemistry measurements identified the potentials for the reversible Fe(III/II) couples for **53** and **46**, substituted with electron withdrawing groups to be more positive than for **14**, with unsubstituted bpy (Table 6). On the other hand, was the same potential for complex **49**, bearing electron donating groups, negatively shifted compared to **14** (Figure 29, Summarized in Table 6).

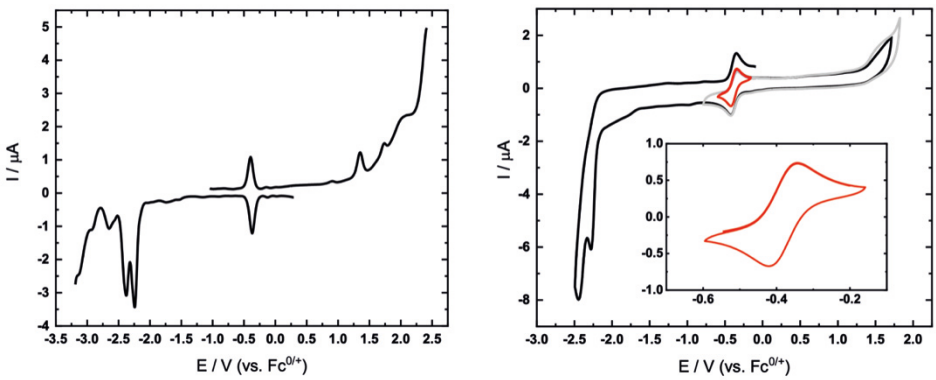

Figure 29 Electrochemistry of 0.38 mM solution of **49** in acetonitrile and 0.1 M TBAPF6 as the electrolyte. Left: Differential pulse voltammograms (step potential: 5 mV, modulation amplitude: 25 mV, modulation time: 50 ms, interval time: 100 ms). Right: Cyclic Voltammograms (scan rate: 0.05 Vs^{-1}; inset: cyclic voltammogram of redox couple).

The shifts in redox potentials between complexes with differently substituted bpy ligands allows for prediction of changes in energy of electronic transitions (for example MLCT) and as a result, shifts of corresponding bands in absorption spectra (Figure 24). Higher ligand reduction potential of **49** (-2.24 V vs. $Fc^{0/+}$) and lower Fe(II/III) oxidation potential (-0.38 V vs. $Fc^{0/+}$) compared to **14** predict higher-energy MLCT bands (hypsochromic shift), which is what is found (λ_{max}(**49**) = 426, 593 nm vs λ_{max}(**14**) = 432, 609 nm). Similarly, bathochromic shifts (lower-energy MLCT) are predicted for **53** and **46** compared to **14**, as is found (Table 6).

Table 6 Summary of redox potentials and absorption maxima of CT states for **14**, **49**, **53** and **46**.

Complex	$E_{1/2}$ (V vs. $Fc^{0/+}$)	Reduction Potentials (V vs. $Fc^{0/+}$)	λ_{max} (MLCT) (nm)	Oxidation Potentials (V vs. $Fc^{0/+}$)	λ_{max} (LMCT) (nm)
14	-0.35	-2.28, -2.42, - 2.64	432, 609	n.a.	n.a.
49	-0.38	-2.24, -2.38, - 2.65	426, 593	1.35, 1.74, 2.09	500, 559, 598
53	-0.34	-2.06, -2.32, - 2.83, -3.10	475, 655	1.34, 1.52, 1.70, 2.06	527, 567, 607
46	-0.30	-2.29, -2.52	509, 661	1.55, 1.86, 2.37	577, 617

Quantum chemical calculations of $\mathbf{53}^{2+}$ and $\mathbf{46}^{2+}$ suggest similar assignments, that the highest-occupied molecular orbital (HOMO) is metal centred, while the lowest unoccupied molecular orbital (LUMO) is ligand centred, more specifically on bpy, suggesting a MLCT state (Figure 30). The calculations also manage to predict the bathochromic shift of the low-energy absorption bands that is found for $\mathbf{53}^{2+}$ and $\mathbf{46}^{2+}$ experimentally.

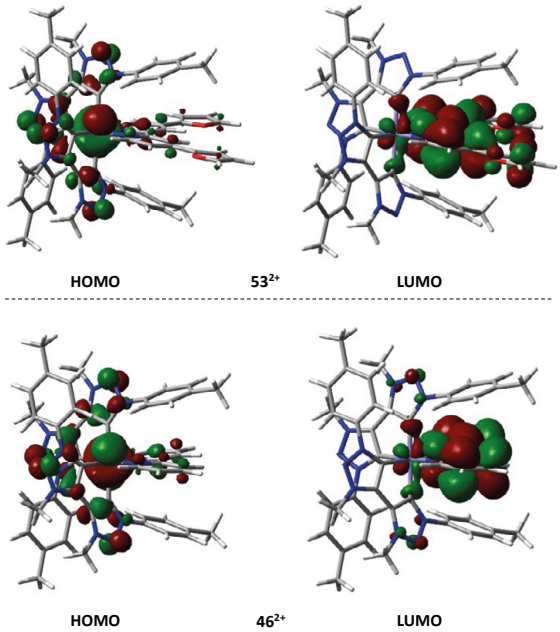

Figure 30 Calculated frontier molecular orbitals. Top left: **53**$^{2+}$ HOMO; top right: **53**$^{2+}$ LUMO; bottom left **46**$^{2+}$ HOMO; bottom right **46**$^{2+}$ LUMO. Results from B3LYP*/6-311G(d,p) in acetonitrile.

The first oxidation potential observed for **49** (1.35 V vs. $Fc^{0/+}$) is not positive enough to give rise to the observed LMCT bands in the absorption spectrum (Figure 31). It is more likely explained by the irreversible Fe(III/IV) redox couple. The same can be claimed for **53** and **46**, where the ligand oxidation potential (LMCT) is not observed in voltammograms.

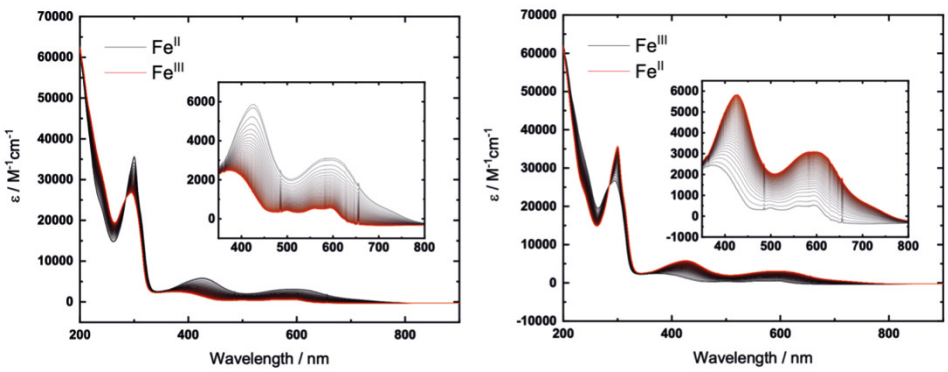

Figure 31 UV-Vis absorption spectra of 0.38 mM solution of **49** in acetonitrile (0.1 M $TBAPF_6$ as the electrolyte) performed by spectroelectrochemistry. Left: oxidation of Fe(II) to Fe(III) (0.5 V; before correction with ferrocene); right: reduction of Fe(III) to Fe(II) (-1 V; before correction with ferrocene).

4.4.3 Magnetic properties

Complexes **14**$^{3+}$, **49**$^{3+}$, **53**$^{3+}$ and **46**$^{3+}$, were all identified as low-spin d^5 complexes in their Fe(III) oxidation state, confirmed by EPR and Mössbauer spectroscopy, as well as with magnetization and magnetic susceptibility measurements (Figure 32), supported by quantum chemical calculations. Paramagnetic shifts in NMR spectra indicate an unpaired electron.

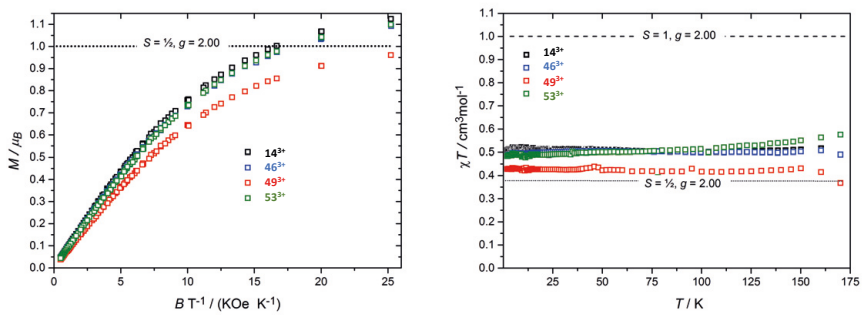

Figure 32 Left: Magnetization data of **14**$^{3+}$, **49**$^{3+}$, **53**$^{3+}$ and **46**$^{3+}$ recorded at temperatures 2-10 K. The superimposable curves for all fields are expected for a non-zero-field-split S = ½ spin-system. Right: Magnetic susceptibility of **14**$^{3+}$, **49**$^{3+}$, **53**$^{3+}$ and **46**$^{3+}$ versus T indicative of an S=½ system with incomplete quenching of the orbital moment.

4.5 Conclusion

The seemingly simple task of replacing unsubstituted bipyridine ligand **15** with carboxylic acid-substituted ligand **40** to obtain **46** instead of **14** proved more complicated due to the simple fact that ligand **40** is insoluble in EtOH. As a result, an alternative synthetic strategy had to be developed, including the synthesis and characterization of new furanyl-substituted ligand **50**. Ultimately, two additional complexes (**49** and **53**) derived from **14** are now a part of a series of complexes that allow for a thorough comparison and estimation of the influence of substitution on the bipyridine ligand on properties of the corresponding iron complexes. Additionally, all four complexes have been isolated and characterised in both Fe(II) and Fe(III) oxidation states. This family of complexes appears to possess redox potentials very close to atmospheric oxygen, since three of the complexes can be oxidised from their stable Fe(II) state by O_2 after a slight lowering of the pH. The fourth complex (**46**) is isolated as an Fe(III) complex and can be reduced to its Fe(II) form, although it is prone to oxidize back to Fe(III).

All complexes have been characterised in their ground state. They were found to be low-spin d^6 (Fe(II)) and d^5 (Fe(III)), as supported by EPR, Mössbauer, magnetic susceptibility measurements and quantum chemical calculations. The ^{1}H NMR

spectra of the Fe(III) complexes were, as expected, paramagnetically shifted, while the ^{1}H resonances of the Fe(II) complexes were unexpectedly broadened. The reason was found computationally and experimentally to be the presence of at least two structurally different energy minima in fast exchange. The exchange could be slowed down by lowering the temperature.

Crystal structures of all four complexes in both oxidation states were obtained through SC-XRD analysis. The crystal structures reveal that there are minimal structural changes induced by changing the substitution on the bipyridine ligand or the oxidation state of the metal. In all cases, the coordination geometry is governed by π-π interactions between aromatic parts of the ligands.

Steady-state absorption spectroscopy revealed that the bipyridine substitution influences the electronics of the ligand π-system, which shifts the energy of absorbed photons and influences the absorption spectra and the perceived color of the complexes. Since both MLCT and LMCT states include excitation to or from ligand-based orbitals with π-symmetry, the excited state dynamics of the complexes are affected by substitution on ligands, although the differences are small. Two of the Fe(III) complexes have shown photoluminescence after having been excited at the appropriate wavelength.

Two of the complexes were found to be dichromatic in their Fe(III) state, where the observed color (hue) is dependent on the path length of travelling light. The phenomenon of dichromatism has been described by referral to the steady-state absorption spectra of these complexes and human physiological response to light.

5 Photoredox catalysis driven with visible light and an Fe-NHC catalyst (Paper IV)

5.1 Background

Following investigations of the influence of changes in the coordination sphere on the properties of various Fe-NHC complexes, potential applications of those complexes have been studied. With careful characterization and mapping of their properties (ES lifetimes, redox potentials, light absorption, etc.), one can match a complex to a research topic of interest. For example, the redox potentials ($E°$(Fe(IV)/Fe*(III)) = -1.88 V vs. $Fc^{+/0}$; $E°$(Fe*(III)/Fe(II)) = 1.0 V vs. $Fc^{+/0}$) and relatively long-lived excited state of **12** (2 ns, ^{2}LMCT) (Figure 33) are of interest when it comes to photoredox catalysis of the base-promoted homolytic aromatic substitution (BHAS) reaction.

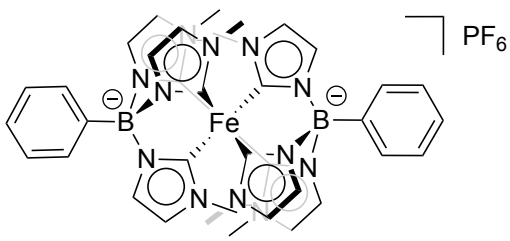

12

τ_0 = 2 ns (^{2}LMCT)

$E°$(Fe(IV)/Fe*(III)) = -1.88 V vs $Fc^{+/0}$
$E°$(Fe*(III)/Fe(II)) = 1.0 V vs $Fc^{+/0}$

Figure 33 The structure of PC **12**, shown along with its ES lifetime and redox potentials.[28]

As the name suggests, BHAS reactions (Scheme 11) are run under basic conditions where a strong base, often *t*-BuOK, is a key component to create an aryl radical intermediate.[74-76] A subsequent intra- or intermolecular, radical reaction with an aromatic C-H unit completes the substitution reaction with the formation of a new C-C bond and the cyclised product (CP, Scheme 11). If the aryl radical intermediates do not form the C-C bond, but react with a hydrogen atom, the hydrogen addition products (HP, Scheme 11), also commonly known as dehalogenated or hydrodehalogenated products, are formed. By taking advantage of the SET step intrinsic to photoredox catalysis, efforts have been made to facilitate the BHAS reaction without employing strongly basic conditions or elevated temperatures. More benign reaction conditions generally reduce the likelihood of decomposition of the reaction components and the complexity of reaction mixtures with fewer unwanted side-reactions. Additionally, in terms of applicability of the method, less basic conditions could increase the functional group tolerance.

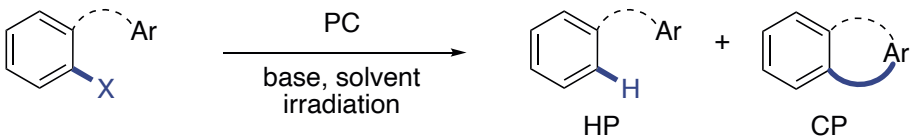

Scheme 11 A general overview of the BHAS reaction, driven by visible light and a photoredox catalyst. X = Br or I.

In the case of an intramolecular BHAS reaction, ring-closure is achieved. Here, two halogen-substituted benzyl core structures (**54** and **58**) (Scheme 12) have been investigated where the benzylic carbon acts as a bridge between the two aromatic ring systems that eventually couple through the BHAS reaction.

5.2 Reaction Optimisation and Validation

Initial reaction optimisations were performed on **54**, screening for conditions where PC **12** could drive the reaction and were found to be (Scheme 12): **54** (50 mM, 1 equiv), **12** (1 mM, 2 mol%), Bu_3N (100 mM, 2 equiv), TMP (2,2,6,6-tetramethylpiperidine, 100 mM, 2 equiv), DMSO-d_6 (2 mL) and green LED irradiation (λ = 530 nm, 3.03 W/vial, 48 h). A photoredox catalytic system previously reported to be driven by a Mo-complex and blue light irradiation (λ = 450 nm)[74] was used as a starting point. The reaction presented in Scheme 12 was run in DMSO-d_6 to be able to monitor the reaction progress directly by ^{1}H NMR spectroscopy. Here, full conversion was observed after 48 hours irradiation time, with the ratio between CP and HP being 75:25. The conversion was monitored by the disappearance of benzylic ^{1}H NMR signals from the crude NMR spectrum of **54**

and the product ratio was determined by integration of benzylic signals originating from CP-**54** and HP-**54**. Further optimisation, using **58** as the substrate, led to a change in the base system; TMP was replaced with K_2CO_3 and only 1 equiv of Bu_3N was needed. These conditions led to 74:26 (CP:HP) product ratio for **58** and an improved 83:17 (CP/HP) ratio for **54**. A series of control reactions were performed to validate the optimised reaction conditions, including replacing or removing the PC, changing or removing the irradiation, replacing the two bases and altering the equivalents used and introducing the radical scavenger (2,2,6,6-Tetramethylpiperidin-1-yl)oxyl (TEMPO). The reaction conditions presented in Scheme 12 were found to produce the highest CP:HP ratio without hampering the reaction.

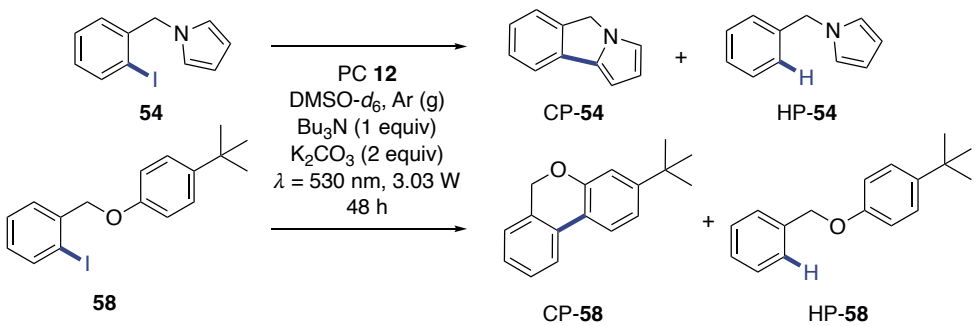

Scheme 12 The optimized reaction conditions for PC **12** using green (λ = 530 nm) light, exemplified with substrates **54** and **58**. The two substrates represent two substrate groups and show the general structure of their CP and HP products.

When 1-(2-iodobenzyl)-1*H*-pyrrole (**54**) and 1-iodo-2-(phenoxymethyl)benzene (**63**) were subjected to the optimised reaction conditions, 5*H*-pyrrolo[2,1-*a*]isoindole (CP-**54**) and 6*H*-benzo[*c*]chromene (CP-**63**) were obtained as the main BHAS products, respectively. The tricyclic CP scaffolds can be found in natural products and pharmaceuticals (Figure 34)[77-79] and are of more value from a synthetic perspective than the HPs that are also produced during the reaction. In addition, dehalogenation of iodoarenes to form HP is a more accessible reaction with various established protocols.[12, 80-81]

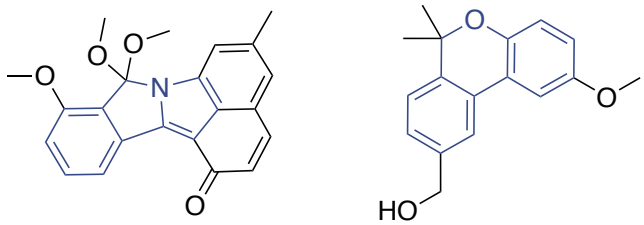

Indole alkaloid 0232A Pulchrol

Figure 34 Examples of natural products that contain the structural scaffolds from CP-**54** and CP-**63** (CP-**59**).

5.3 Substrate scope

The substrate scope shown in Figure 35 features phenol- and pyrrole-substituted halobenzylic substrates which serves to evaluate the effect of the functionality, length and orientation of the sp^3-hybridized bridge, the size of π-system and the choice of halogen substituent on the BHAS reaction.

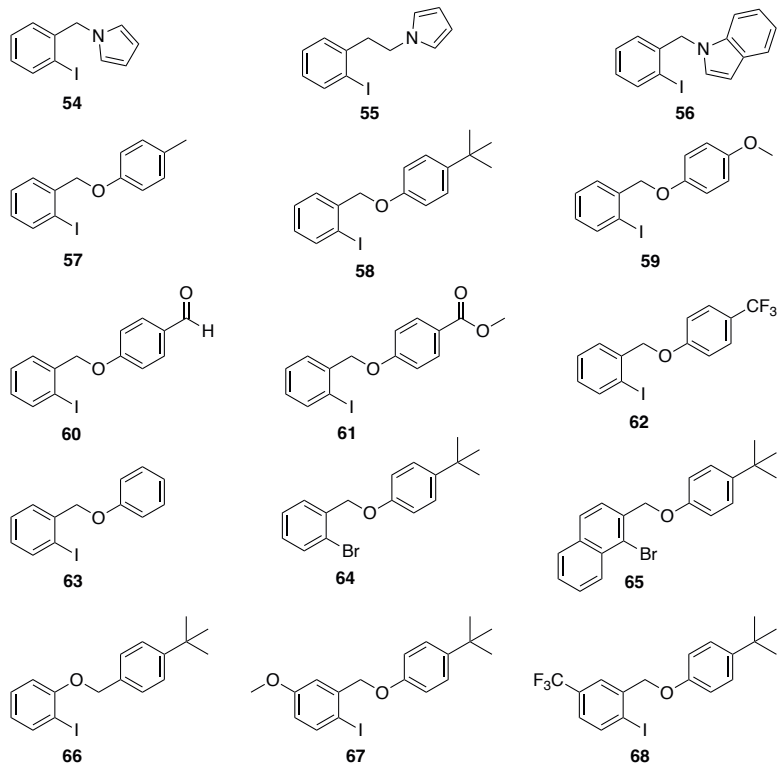

Figure 35 The substrate scope planned to investigate the BHAS reaction driven by green (λ = 530 nm) light and PC **12**

Pyrrole substrate **54** compares to its derivative **55** with an additional sp^3-hybridized carbon separating the two aromatic rings, expanding the size of the formed ring from five to six atoms. In addition, the pyrrole of **54** was exchanged for indole in substrate **56**, where selectivity between two C-H moieties on the indole arises, leading to 5-(CP5-**56**) or 6-membered (CP6-**56**) ring formations (Scheme 13).

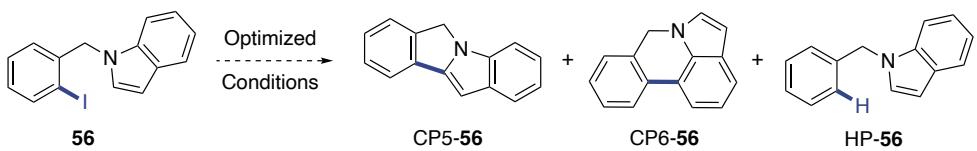

Scheme 13 Potential product mixture from BHAS reaction of substrate **56**. Two CPs could theoretically be formed, potentially providing selectivity information.

The remainder of the substrates have a benzyloxy unit bridging two aromatic rings. To investigate the effect of the electron density on the non-halogenated aromatic

ring, it was substituted with electron-donating (**57-59**) and electron-withdrawing (**60-62**) functional groups and compared to the substrate featuring an unsubstituted phenyl ring, **63**. Substitution in the position para to the methoxy bridge is known to have the largest effect on the electron density.[82] The influence of the halogen was evaluated with substrates **64** and **65**. Substrate **66** was used to investigate the effect of inverting the benzyloxy bridge (compared to substrate **58**). Finally, the effect of electron density on the halogen bearing phenyl ring was investigated with electron-donating (**67**) and electron-withdrawing (**68**) groups positioned para to the halogen atom.

5.4 Substrate synthesis

One part of the project was the efficient synthesis of substrates to investigate BHAS reaction. Pyrrole-containing substrate **54** was made through an S_N2 reaction between iodobenzylbromide (**69**) and pyrrole (Scheme 14).[74]

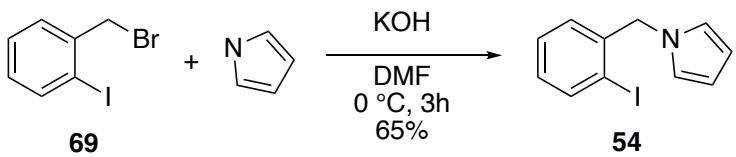

Scheme 14 The synthesis of substrate **54** from iodobenzylbromide **69** and pyrrole.[74]

The pyrrole-containing substrate with an extra carbon in the saturated linker (**55**) cannot be made efficiently with an S_N2 reaction and requires an alternative strategy of three steps (Scheme 15).[74, 83] The fact that the N-containing substrates degrade over time necessitated preparation of those shortly before they were subjected to photocatalytic investigation. For that reason, 2-(2-iodophenyl)acetonitrile (**70**), made from **69**, has not been reacted further. In due course, **55** can be synthesized by the reduction of **70** to primary amine **71**, followed by a condensation reaction to form the pyrrole unit.

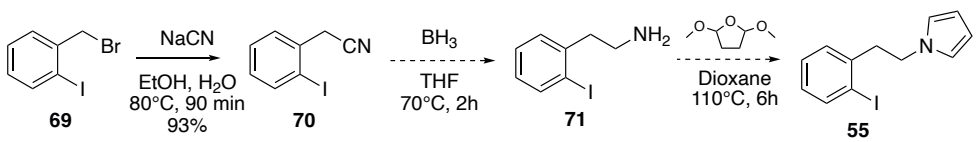

Scheme 15 Planned three-step synthesis of substrate **55**.[74, 83] Only the first step has been completed thus far, owing to the degradation of substrate **55** and intermediate **71** when stored.

Ten substrates from the substrate scope were obtained through an S_N2 reaction between a phenol and bromobenzyl moiety following a reported procedure[84] in very good to excellent yields (Table 7). For one of the substrates (**67**), the bromobenzyl unit **74** was made through a two-step synthesis; arene iodination of **72**, followed by a PBr_3 bromination of a primary alcohol **73** (Scheme 16).[85]

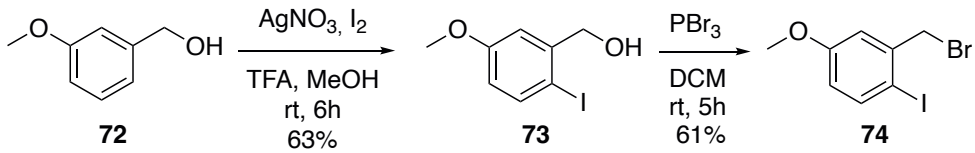

72 **73** **74**

Scheme 16 The two-step synthesis of benzylbromide **74**, a reagent for the synthesis of substrate **67**, starting from anisole **72**.[85]

Table 7 The conditions and results of the syntheses of substrates **57**-**64** and **67**-**68**.[84]

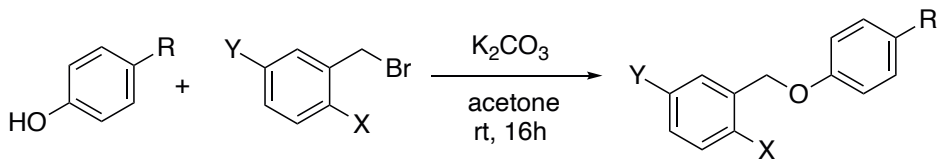

Substrate	R	X	Y	Yield
57	-Me	-I	-H	83%
58	-*t*-Bu	-I	-H	99%
59	-OMe	-I	-H	82%
60	-CHO	-I	-H	88%
61	-COOMe	-I	-H	87%
62	$-CF_3$	-I	-H	94%
63	-H	-I	-H	97%
64	-*t*-Bu	-Br	-H	93%
67	-*t*-Bu	-I	-OMe	89%
68	-*t*-Bu	-I	$-CF_3$	94%

The two remaining substrates from the substrate scope, **65** and **66** were synthesized through similar S_N2 reactions (Scheme 17).

Out of the 15 substrates, **61**, **65** and **67** have not been reported in the literature and were therefore fully characterized by CHN elemental analysis, HR-MS analysis and NMR spectroscopy.

5.5 Photoredox Catalysis and Product Isolation

Table 8 describes the results of the photocatalytic BHAS reaction of the chosen substrate scope that have been obtained to this point. In some cases, significant amounts of substrate remained after the 48 h reaction time. These photoreactions were allowed to react further, until full consumption of the substrate was observed by ^{1}H NMR analysis. Otherwise, the beforementioned optimised reaction conditions were applied to all substrates. ^{1}H NMR analysis was used to determine the product ratio as well as the NMR yield, using 1,3,5-trimethoxybenzene as an internal standard (IS). Isolated yields were determined after successful product purification and isolation.

Table 8 Converstion of substrates, product ratios and yields for the BHAS reaction on substrates from the planned scope. NMR yields were determined using 1,3,5-trimethoxybenzene as an internal standard. n.d. = not determined; n.a. = not applicable;

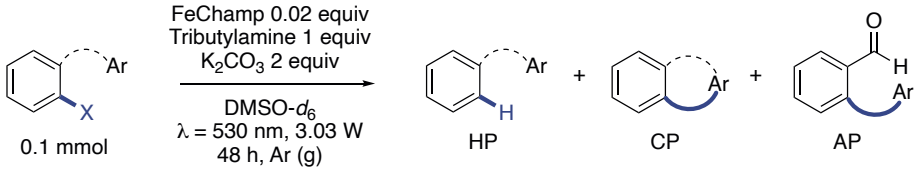

Substrate	Conversion	^{1}H-NMR product ratio CP:HP(:AP)	Yield % (^{1}H NMR, isolated)		
			CP	HP	AP
54	100	83:17	77, 59	16, 11	n.a.
55	n.d.	n.d.	n.d.	n.d.	n.d.
56	n.d.	n.d.	n.d.	n.d.	n.d.
57	100	64:28:8	52, 26	21, 9	n.d.
58	100	66:23:11	53, 46	19, 23	n.d.
59	100	70:16:14	58, 35	13, 8	n.d.
60	n.d.	n.d.	n.d.	n.d.	n.d.
61	n.d.	n.d.	n.d.	n.d.	n.d.
62	100	68:32	66, n.d.	10, n.d.	n.a.
63	100	65:29:6	55, 30	26, 6	n.d.
64	0	-	-	-	
65	100	44:7:49	34, 23	5, 3	n.d.
66	100 (140 h)	77:23	39, n.d.	12, n.d.	n.a.
67	n.d.	n.d.	n.d.	n.d.	n.d.
68	100	91:6:3	68, n.d.	4, n.d.	n.d.

The product ratio from the BHAS reaction of **54** was found to be 83:17 (CP/HP), which was the most favorable ratio observed thus far. In this case, the ^{1}H NMR yields and isolated yields are relatively high as well. Related substrates **55** and **56** have not been investigated yet. Of the substrates bearing the benzyloxy bridge, the three substrates substituted with electron-donating functional groups, **57**-**59**, and the

unsubstituted **63** have similar product ratios, ^{1}H NMR and isolated yields. Interestingly, the ^{1}H NMR spectra of the crude product mixtures of these four substrates also show signals from a third structure, which features an aldehyde and no benzylic protons. The chemical structure and formation of this aldehyde product (AP) will be described in more detail in relation to the mechanistic discussion in the following section. The AP was not observed for any of the substrates substituted with electron-withdrawing functional groups (**60-62**). Unreacted substrate **61** was found in substantial amounts in the crude ^{1}H NMR after 48-hour irradiation and 100 hours were found to be needed to reach full conversion. Another substrate that required extended reaction times was **66**, where 140 h reaction time resulted in near full consumption of the starting substrate. The prolonged exposure to strong irradiation was found to negatively affect the observed product yields, for both CP and HP, while additionally contributing to more side reactivity and more complex crude reaction mixtures. Exchanging the iodine for bromine inhibits any reaction, as seen for substrate **64**. The C-Br bond is stronger than the C-I bond and formation of the aryl radical by breaking the C-X bond is suppressed. This is supported by the full recovery of the substrate. By expanding the π-system of the Br-bearing arene, from benzene to naphthalene, the radical BHAS mechanism can be initiated and full conversion of starting substrate **65** is achieved in 48 h. The CP-HP ratio is low, as well as the yields (^{1}H NMR and isolated), which can be explained by the formation of a substantial amount of AP which is, according to ^{1}H NMR analysis, the main product of the reaction.

5.6 Mechanism

By transient absorption kinetics, the ES lifetime of PC **12** was estimated to be 1.43 ns in DMSO, slightly shorter than the 2 ns lifetime reported in acetonitrile.[28] Bimolecular emission quenching studies of ES PC **12*** by various substrates (**54**, **58** and **66**) revealed that minimal or no oxidative quenching of the ES was observed. As a result, charge separated products were not observed following oxidative quenching which rendered determination of cage escape yields impossible. Substrate **54**, along with 1-methylpyrrole and benzylpyrrole show some reductive quenching by the pyrrole unit. The sacrificial electron donor (SED) Bu_3N was found to reductively quench **12*** to form a radical cation and after deprotonation, the resulting α-aminoalkyl radical can participate in either SET or halogen atom transfer (XAT) with the C-X bond of a substrate to initiate the radical mechanism (Scheme 17).[86-87]

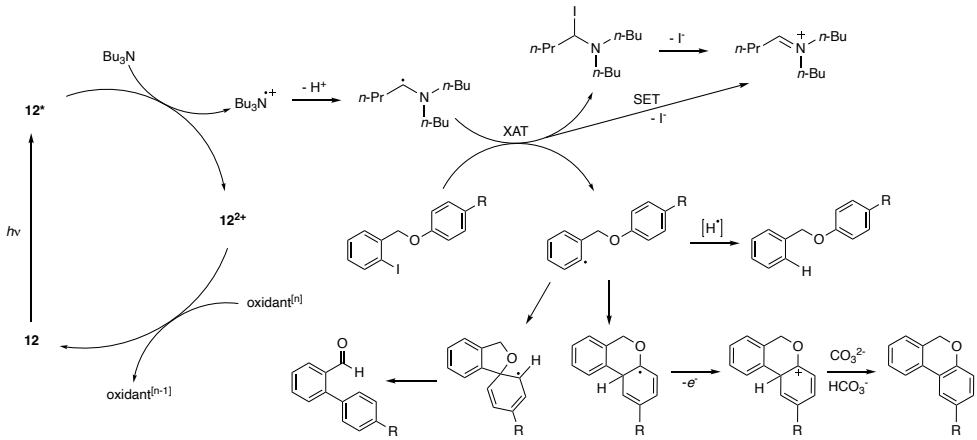

Scheme 17 Proposed reaction mechanism for the BHAS reaction driven by PC **12** and green (λ = 530 nm) light.

By varying the equivalents of Bu_3N in the reaction mixture and by adding radical scavenger TEMPO, the presence of a radical chain propagation pathway was supported (Scheme 18).

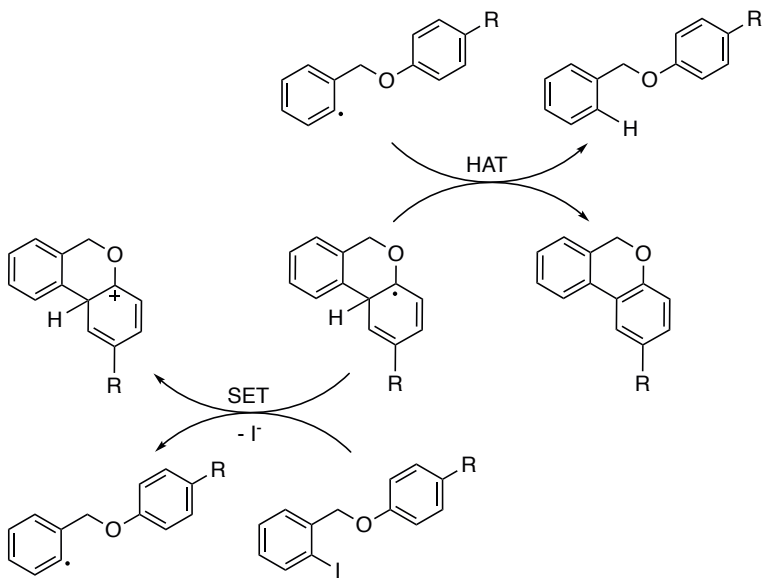

Scheme 18 Proposed radical chain propagation pathways for the BHAS reaction.

Upon formation, the aryl radical can accept an electron and a proton, consecutively or simultaneously, through hydrogen atom transfer (HAT), to form the HP.

Alternatively, the aryl radical can ring-close in an intramolecular (6-*endo*-trig, 5-*endo*-trig for **54**-**56**) fashion to form a reactive chromene (isoindole for **54**-**56**) radical, which then leads to CP through single electron oxidation, followed by deprotonation of the formed cationic intermediate. For some substrates (**57**-**60** and **65**) an alternative ring-closure (5-*exo*-trig) is proposed (Scheme 19) which leads to the observed AP. A molecular modelling study of the two proposed ring-closing pathways has been reported previously,[82] where the conclusion is that the 6-*endo* pathway is kinetically favoured since the 5-*exo* pathway transition state is generally higher in energy than the 6-*endo*. The radical intermediate originating from 5-*exo* cyclisation is, however, lower in energy than the corresponding 6-*endo* intermediate. Our results can be explained with the reported modelling of the cyclization. For substrates where no AP is observed, the energy difference between the 5-*exo* and 6-*endo* transition states could be too large for the 5-*exo* pathway to proceed. When the electron density of the phenyloxy ring is increased through substitution, the transition states of the two cyclization pathways are brought energetically closer together, which opens up the 5-*exo* pathway. For substrate **65**, AP-**65** is formed in at least equal amounts as CP-**65**, which could imply that the 5-*exo* and 6-*endo* transition states are close in energy. This indicates that the aromatic system of the benzyloxy radical plays an important role in the energies of the transition states. Substrates **67** and **68** will undoubtedly contribute to better understanding of the influence of substituents on the observed reactivity. There is no mention of AP in the work on relative energies of the transition states, however, a CP regioisomer, CP', resulting from a ring expansion of the spiro radical compound formed by the 5-*exo* cyclisation was observed.[82] This indicates that the more benign conditions we have developed allow for the formation of the observed AP, which is not seen in conditions that utilize strong base systems and irradiation of higher energy. To the best of our knowledge, formation of such aldehyde species through a photoinduced process has not been reported before. With further investigations of the mechanism of AP formation and reaction optimization for the AP, there could be potential synthetic applications for such rearrangements.

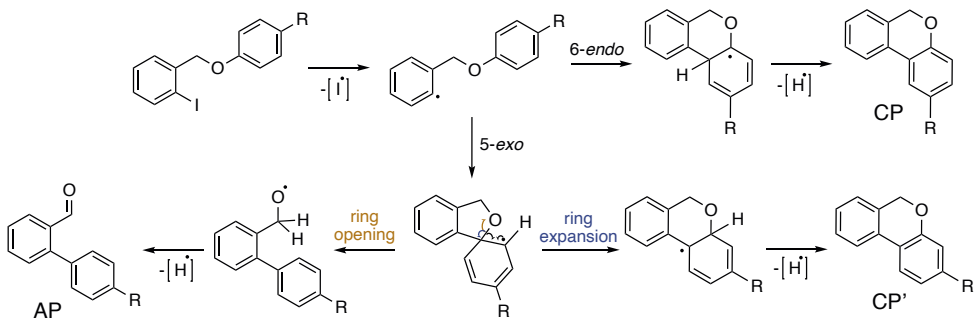

Scheme 19 Proposed photoinduced formation pathway of observed AP in the BHAS reaction, through a 5-exo-trig ring closing step.

5.7 Conclusion

The function of **12** as a PC in intramolecular BHAS reactions has been successfully established, employing green light (λ = 530 nm), a mild base (K_2CO_3) and a SED (Bu_3N). A substrate scope was established and synthesized, including three new substrates which were carefully characterized. The investigated BHAS reaction resulted in the predominant formation of the more synthetically valuable CP over HP. This methodology offers a novel, more benign approach to the well-known BHAS reaction, no longer excluding substrates that feature base-sensitive functional groups such as aldehydes and esters. A reaction mechanism was proposed, which was supported by experiments and could explain the unexpected finding of the formation of AP for some substrates. These findings contribute to the expanding field of iron photoredox catalysis as a whole, and invites continued discovery and exploration of new applications for Fe-NHC PCs in photoredox catalysis.

6 Concluding remarks

The work presented in this thesis describes the investigation of the reactivity and properties of Fe-NHC complexes. A group of new complexes have been synthesized and characterized in an attempt to better understand their structure-property relationships and how synthetic design can aid in the search of complexes with properties desired for photocatalytic or photovoltaic applications.

The synthesis of most of the iron complexes is based on previously reported synthesis of heteroleptic complex **14**, in a two-step process, through high-spin intermediate complex [$FeCl_2$(N-N')]. The small reaction scope, limited by solubility in EtOH, and instability of the intermediate has prevented simple adaptation of the reported procedure. However, this led to development of synthetic strategies and larger pool of new, heteroleptic Fe-NHC complexes, allowing for better comparison and more thorough understanding of the systems presented in this work. Some of the complexes discussed here have shown unexpected properties, which have been explained by experimental and theoretical investigations.

In the last part of the thesis, application of an Fe-NHC complex (**12**) as a photoredox catalyst to drive a chemical reaction with green light is presented. While irradiation of lower energy and milder conditions than for conventional methods to catalytically perform the reaction are needed, this photoredox catalyst has shown that Fe-NHC complexes can offer value as unconventional photocatalysts. With complex **46** and its carboxylic acid groups in hand, photovoltaic performance can now be investigated. The broad absorbance over most of the visible part of the electromagnetic spectrum is promising but rather short excited state lifetime might limit applicability.

The results of this thesis will hopefully encourage continued exploration of the relationship between structure and properties of Fe-NHC complexes towards more complete understanding of their chemistry and application within the field of photochemistry.

7 Acknowledgements

During my PhD studies I have met and worked with uncountable number of brilliant individuals. At home I have my safety net of family and friends that have helped me with whatever I have needed, whenever I needed. This thesis and the work presented within was made possible by this amazing group of people and I would like to express my sincere gratitude to all of them.

Thank you, KENNETH, for the trust that you have shown me by offering me opportunity to pursue a PhD in your group. I am grateful for your constant encouragement and support where I have grown incredibly as a researcher and a person.

Thank you, OLA (co-supervisor), PATRIC (department representative) and VIVEKA (study director). You have made sure I was on the right track and offered valuable help, support and input to bring me here.

Special thank you, JÓHANNA for designing and making the front cover of my thesis. SAMUEL, LISA and ANNA for proofreading my thesis.

Thank you, past and present members of the KW group. ANNA, LISA, ALEKS, JESPER, SAMUEL, ERIC, CLARA, VICKY for sharing everything the PhD studies have to offer with me. You have been my collegues, friends, inspiration, voices of reason and much more! HAILIANG, OLGA, SAMI for your help when I was starting my PhD. OM, KUMKUM, SIMON K, ESMAEIL, ALPESH, ARVIND, DNYANESHWAR, SURESH, YOGESH and ABHISHEK for your endless support when I was struggling in the laboratory. I could always ask for help, theoretical, technical or emotional. My army of Tröger's base students, for nice collaboration and giving me the great joy to exchange knowledge and experience.

Thank you, collaborators and co-authors. PAVEL, CATHERINE, MAWULI, LINNEA, NILS, NIDHI, IRIA, YEN, ARKADY, REINER, PETTER, ELENA for our collaboration and pleasant exchange of ideas, knowledge and experience.

Thank you, past and present members at CAS for making it enjoyable and rewarding for me to go to work every day. Special thanks to; MARIA, SARA, KORNELIJE and ULF D for keeping the place running and all the amazing support and help. SOFIA, ANETTE and FIONA for the help with mass spectrometry. KARL-ERIK and ZOLTAN for your NMR expertise and enthusiastic help. DANIEL and ARVIND for XRD and the patience when I brought you endless batches of difficult crystals. KARL-ERIK,

Peter, Olivier, Tamani, Smita, Vicky and all other members of the Feel-Good committee for our joint effort to bring up the spirit of the unit.

Thank you, my friends. Many of the people I have mentioned thus far I can proudly call my friends. Magnús, Sigmar for always being there for a chat, laugh, computer games or very important football discussions. Aníta, Jóhanna, Sólrún, Rakel, Fríða for making up the group of long-time friends and always being prepared to meet and catch-up. Bianca, Edward, Larissa for all the games we have played, amazing food (except the mushrooms), cakes and snacks. Icelandic Stångby/Tetra Pak football team for all the late Tuesday evening/Sunday morning football and the yearly celebration!

Takk Mamma, Pabbi, Brynja, Bjarki, Sæbjörg, Amma, Afi, Sesselja og Halli fyrir alla samveruna, heimsóknirnar, stuðninginn og hjálpina yfir hafið. Ferðalagið hefur alltaf verið þess virði!

Takk Gunnhildur! Eiginkona, barnsmóðir, drifkraftur og kletturinn í mínu lífi. Þú hefur alltaf verið til staðar fyrir mig og fært miklar fórnir til þess að hjálpa mér með lífið og doktorsnámið, fyrir það verð ég ævinlega þakklátur. Ég elska þig og fjölskylduna okkar ♥ Þú ert hetjan mín!

8 References

1. Institute, E., *Statistical Review of World Energy. 72,* **2023**
2. Williams, D., *Sun Fact Sheet* In Planetary Fact Sheets. NASA; Last updated: 17 November **2022.** Accessed: [05 January 2024]
3. Morton, O., *Nature* **2006**, *443* (7107), 19-22.
4. Abrahamsson, M., In *Photochemistry* ed., 44; Fasani, E.; Albini, A., Eds.; The Royal Society of Chemistry: Cambridge, UK, **2017**, 285-295.
5. Hagfeldt, A.; Grätzel, M., *Acc. Chem. Res.* **2000**, *33* (5), 269-277.
6. Efaz, E. T.; Rhaman, M. M.; Imam, S. A.; Bashar, K. L.; Kabir, F.; Mourtaza, M. D. E.; Sakib, S. N.; Mozahid, F. A., *Engineering Research Express* **2021**, *3* (3), 032001.
7. O'Regan, B.; Grätzel, M., *Nature* **1991**, *353* (6346), 737-740.
8. Grätzel, M., *Journal of Photochemistry and Photobiology C: Photochemistry Reviews* **2003**, *4* (2), 145-153.
9. Hagfeldt, A.; Boschloo, G.; Sun, L.; Kloo, L.; Pettersson, H., *Chem. Rev.* **2010**, *110* (11), 6595-6663.
10. Michaels, H.; Benesperi, I.; Freitag, M., *Chem. Sci.* **2021**, *12* (14), 5002-5015.
11. Prier, C. K.; Rankic, D. A.; MacMillan, D. W. C., *Chem. Rev.* **2013**, *113* (7), 5322-5363.
12. Nguyen, J. D.; D'Amato, E. M.; Narayanam, J. M. R.; Stephenson, C. R. J., *Nature chemistry* **2012**, *4* (10), 854-859.
13. Haynes, W. M. (Ed.), **2016,** *CRC Handbook of Chemistry and Physics* (97th edition), CRC Press: Boca Raton.
14. Wenger, O. S., *Chem. - Eur. J.* **2019**, *25* (24), 6043-6052.
15. Pyykko, P., *Chem. Rev.* **1988**, *88* (3), 563-594.
16. Kaupp, M., *J. Comput. Chem.* **2007**, *28* (1), 320-325.
17. McCusker, J. K., *Science* **2019**, *363* (6426), 484-488.
18. Liu, Y.; Persson, P.; Sundström, V.; Wärnmark, K., *Acc. Chem. Res.* **2016**, *49* (8), 1477-1485.
19. Herrmann, W. A.; Köcher, C., *Angew. Chem. Int. Ed. Engl.* **1997**, *36* (20), 2162-2187.
20. Velazquez, H. D.; Verpoort, F., *Chem. Soc. Rev.* **2012**, *41* (21), 7032-7060.
21. Vellé, A.; Cebollada, A.; Macías, R.; Iglesias, M.; Gil-Moles, M.; Sanz Miguel, P. J., *ACS Omega* **2017**, *2* (4), 1392-1399.
22. Herrmann, W. A., *Angew. Chem. Int. Ed.* **2002**, *41* (8), 1290-1309.
23. Hopkinson, M. N.; Richter, C.; Schedler, M.; Glorius, F., *Nature* **2014**, *510* (7506), 485-496.

24. Crabtree, R., *The organometallic chemistry of the transition metals*. John Wiley & Sons, Inc.: NJ, USA, **2019**.
25. Liu, Y.; Kjær, K. S.; Fredin, L. A.; Chábera, P.; Harlang, T.; Canton, S. E.; Lidin, S.; Zhang, J.; Lomoth, R.; Bergquist, K.-E.; Persson, P.; Wärnmark, K.; Sundström, V., *Chem. - Eur. J.* **2015**, *21* (9), 3628-3639.
26. Chábera, P.; Kjaer, K. S.; Prakash, O.; Honarfar, A.; Liu, Y.; Fredin, L. A.; Harlang, T. C. B.; Lidin, S.; Uhlig, J.; Sundström, V.; Lomoth, R.; Persson, P.; Wärnmark, K., *J. Phys. Chem. Lett.* **2018**, *9* (3), 459-463.
27. Chábera, P.; Liu, Y.; Prakash, O.; Thyrhaug, E.; Nahhas, A. E.; Honarfar, A.; Essén, S.; Fredin, L. A.; Harlang, T. C. B.; Kjær, K. S.; Handrup, K.; Ericson, F.; Tatsuno, H.; Morgan, K.; Schnadt, J.; Häggström, L.; Ericsson, T.; Sobkowiak, A.; Lidin, S.; Huang, P.; Styring, S.; Uhlig, J.; Bendix, J.; Lomoth, R.; Sundström, V.; Persson, P.; Wärnmark, K., *Nature* **2017**, *543* (7647), 695-699.
28. Kjær, K. S.; Kaul, N.; Prakash, O.; Chábera, P.; Rosemann, N. W.; Honarfar, A.; Gordivska, O.; Fredin, L. A.; Bergquist, K.-E.; Häggström, L.; Ericsson, T.; Lindh, L.; Yartsev, A.; Styring, S.; Huang, P.; Uhlig, J.; Bendix, J.; Strand, D.; Sundström, V.; Persson, P.; Lomoth, R.; Wärnmark, K., *Science* **2019**, *363* (6424), 249-253.
29. Chábera, P.; Lindh, L.; Rosemann, N. W.; Prakash, O.; Uhlig, J.; Yartsev, A.; Wärnmark, K.; Sundström, V.; Persson, P., *Coord. Chem. Rev.* **2021**, *426*, 213517.
30. Fredin, L. A.; Pápai, M.; Rozsályi, E.; Vankó, G.; Wärnmark, K.; Sundström, V.; Persson, P., *J. Phys. Chem. Lett.* **2014**, *5* (12), 2066-2071.
31. Kaufhold, S.; Wärnmark, K., *Catalysts* **2020**, *10* (1), 132.
32. Young, E. R.; Oldacre, A., *Science* **2019**, *363* (6424), 225-226.
33. Abrahamsson, M.; Jäger, M.; Österman, T.; Eriksson, L.; Persson, P.; Becker, H.-C.; Johansson, O.; Hammarström, L., *J. Am. Chem. Soc.* **2006**, *128* (39), 12616-12617.
34. Jäger, M.; Smeigh, A.; Lombeck, F.; Görls, H.; Collin, J.-P.; Sauvage, J.-P.; Hammarström, L.; Johansson, O., *Inorg. Chem.* **2010**, *49* (2), 374-376.
35. Liu, L.; Duchanois, T.; Etienne, T.; Monari, A.; Beley, M.; Assfeld, X.; Haacke, S.; Gros, P. C., *Physical Chemistry Chemical Physics* **2016**, *18* (18), 12550-12556.
36. Srivastava, V.; Singh, P. P., *RSC Advances* **2017**, *7* (50), 31377-31392.
37. Pirtsch, M.; Paria, S.; Matsuno, T.; Isobe, H.; Reiser, O., *Chem. - Eur. J.* **2012**, *18* (24), 7336-7340.
38. Fajardo, J., Jr.; Barth, A. T.; Morales, M.; Takase, M. K.; Winkler, J. R.; Gray, H. B., *J. Am. Chem. Soc.* **2021**, *143* (46), 19389-19398.
39. Cheung, K. P. S.; Sarkar, S.; Gevorgyan, V., *Chem. Rev.* **2022**, *122* (2), 1543-1625.
40. Romero, N. A.; Nicewicz, D. A., *Chem. Rev.* **2016**, *116* (17), 10075-10166.
41. Arias-Rotondo, D. M.; McCusker, J. K., *Chem. Soc. Rev.* **2016**, *45* (21), 5803-5820.
42. Marzo, L.; Pagire, S. K.; Reiser, O.; König, B., *Angew. Chem. Int. Ed.* **2018**, *57* (32), 10034-10072.
43. Zhang, J.; Campolo, D.; Dumur, F.; Xiao, P.; Fouassier, J. P.; Gigmes, D.; Lalevée, J., *J. Polym. Sci., Part A: Polym. Chem.* **2016**, *54* (14), 2247-2253.
44. Lin, I. J. B.; Vasam, C. S., *Coord. Chem. Rev.* **2007**, *251* (5), 642-670.
45. Duchanois, T.; Etienne, T.; Beley, M.; Assfeld, X.; Perpète, E. A.; Monari, A.; Gros, P. C., *Eur. J. Inorg. Chem.* **2014**, *2014* (23), 3747-3753.

46. Lindh, L.; Gordivska, O.; Persson, S.; Michaels, H.; Fan, H.; Chábera, P.; Rosemann, N. W.; Gupta, A. K.; Benesperi, I.; Uhlig, J.; Prakash, O.; Sheibani, E.; Kjaer, K. S.; Boschloo, G.; Yartsev, A.; Freitag, M.; Lomoth, R.; Persson, P.; Wärnmark, K., *Chem. Sci.* **2021**, *12* (48), 16035-16053.
47. Charron, F. F., Jr.; Reiff, W. M., *Inorg. Chem.* **1986**, *25* (16), 2786-2790.
48. Kalyanasundaram, K.; Kiwi, J.; Grätzel, M., *Helv. Chim. Acta* **1978**, *61* (7), 2720-2730.
49. Brown, G. M.; Brunschwig, B. S.; Creutz, C.; Endicott, J. F.; Sutin, N., *J. Am. Chem. Soc.* **1979**, *101* (5), 1298-1300.
50. Crutchley, R. J.; Lever, A. B. P., *J. Am. Chem. Soc.* **1980**, *102* (23), 7128-7129.
51. Canton, S. E.; Zhang, X.; Zhang, J.; van Driel, T. B.; Kjaer, K. S.; Haldrup, K.; Chabera, P.; Harlang, T.; Suarez-Alcantara, K.; Liu, Y.; Pérez, J.; Bordage, A.; Pápai, M.; Vankó, G.; Jennings, G.; Kurtz, C. A.; Rovezzi, M.; Glatzel, P.; Smolentsev, G.; Uhlig, J.; Dohn, A. O.; Christensen, M.; Galler, A.; Gawelda, W.; Bressler, C.; Lemke, H. T.; Møller, K. B.; Nielsen, M. M.; Lomoth, R.; Wärnmark, K.; Sundström, V., *J. Phys. Chem. Lett.* **2013**, *4* (11), 1972-1976.
52. Cotton, F. A.; Luck, R. L.; Son, K.-A., *Inorg. Chim. Acta* **1991**, *179* (1), 11-15.
53. Brechin, E. K.; Calucci, L.; Englert, U.; Margheriti, L.; Pampaloni, G.; Pinzino, C.; Prescimone, A., *Inorg. Chim. Acta* **2008**, *361* (8), 2375-2384.
54. Song, Y.-F.; Yang, P., *Polyhedron* **2001**, *20* (6), 501-506.
55. Vezzu, D. A. K.; Ravindranathan, D.; Garner, A. W.; Bartolotti, L.; Smith, M. E.; Boyle, P. D.; Huo, S., *Inorg. Chem.* **2011**, *50* (17), 8261-8273.
56. Mengel, A. K. C.; Förster, C.; Breivogel, A.; Mack, K.; Ochsmann, J. R.; Laquai, F.; Ksenofontov, V.; Heinze, K., *Chem. - Eur. J.* **2015**, *21* (2), 704-714.
57. Moll, J.; Naumann, R.; Sorge, L.; Förster, C.; Gessner, N.; Burkhardt, L.; Ugur, N.; Nuernberger, P.; Seidel, W.; Ramanan, C.; Bauer, M.; Heinze, K., *Chem. - Eur. J.* **2022**, *28* (57), e202201858.
58. Cheng Yong, S. L., *Chin. J. Org. Chem.* **2012**, (03), 511-519.
59. Weiss, D. T.; Altmann, P. J.; Haslinger, S.; Jandl, C.; Pöthig, A.; Cokoja, M.; Kühn, F. E., *Dalton Trans.* **2015**, *44* (42), 18329-18339.
60. Liang, Q.; Janes, T.; Gjergji, X.; Song, D., *Dalton Trans.* **2016**, *45* (35), 13872-13880.
61. Gardiner, M. G.; Ho, C. C., *Coord. Chem. Rev.* **2018**, *375*, 373-388.
62. Hohloch, S.; Suntrup, L.; Sarkar, B., *Organometallics* **2013**, *32* (24), 7376-7385.
63. Darari, M.; Francés-Monerris, A.; Marekha, B.; Doudouh, A.; Wenger, E.; Monari, A.; Haacke, S.; Gros, P. C., *Molecules* **2020**, *25* (24), 5991.
64. Lundqvist, M. J. *Quantum Chemical Modeling of Dye-Sensitized Titanium Dioxide: Ruthenium Polypyridyl and Perylene Dyes, TiO2 Nanoparticles, and Their Interfaces*. PhD Dissertation. **2006.** Uppsala University, Uppsala.
65. Österman, T.; Abrahamsson, M.; Becker, H.-C.; Hammarström, L.; Persson, P., *J. Phys. Chem. A* **2012**, *116* (3), 1041-1050.
66. Fredin, L. A.; Wallenstein, J.; Sundin, E.; Jarenmark, M.; Barbosa de Mattos, D. F.; Persson, P.; Abrahamsson, M., *Inorg. Chem.* **2019**, *58* (24), 16354-16363.
67. Duchanois, T.; Etienne, T.; Cebrián, C.; Liu, L.; Monari, A.; Beley, M.; Assfeld, X.; Haacke, S.; Gros, P. C., *Eur. J. Inorg. Chem.* **2015**, *2015* (14), 2469-2477.

68. Miyaura, N.; Yamada, K.; Suzuki, A., *Tetrahedron Lett.* **1979**, *20* (36), 3437-3440.
69. Miyaura, N.; Suzuki, A., *J. Chem. Soc., Chem. Commun.* **1979**, (19), 866-867.
70. Miyaura, N.; Suzuki, A., *Chem. Rev.* **1995**, *95* (7), 2457-2483.
71. *The Merck Index - 10th Ed.* Merck & Co., Inc: **1983**.
72. Carey, M. C.; Adelman, Sara L.; McCusker, J. K., *Chem. Sci.* **2019**, *10* (1), 134-144.
73. Kreft, S.; Kreft, M., *Naturwissenschaften* **2007**, *94* (11), 935-939.
74. Herr, P.; Glaser, F.; Büldt, L. A.; Larsen, C. B.; Wenger, O. S., *J. Am. Chem. Soc.* **2019**, *141* (36), 14394-14402.
75. Budén, M. E.; Guastavino, J. F.; Rossi, R. A., *Org. Lett.* **2013**, *15* (6), 1174-1177.
76. Studer, A.; Curran, D. P., *Angew. Chem. Int. Ed.* **2011**, *50* (22), 5018-5022.
77. Kleinwächter, P.; Schlegel, B.; Groth, I.; Härtl, A.; Gräfe, U., *J. Antibiot.* **2001**, *54* (6), 510-512.
78. Pratap, R.; Ram, V. J., *Chem. Rev.* **2014**, *114* (20), 10476-10526.
79. Erosa-Rejón, G. J.; Yam-Puc, A.; Chan-Bacab, M. J.; Giménez-Turbax, A.; Salamanca, E.; Peña-Rodríguez, L. M.; Sterner, O., *Phytochem. Lett.* **2010**, *3* (1), 9-12.
80. Aydogan, A.; Bangle, R. E.; Cadranel, A.; Turlington, M. D.; Conroy, D. T.; Cauët, E.; Singleton, M. L.; Meyer, G. J.; Sampaio, R. N.; Elias, B.; Troian-Gautier, L., *J. Am. Chem. Soc.* **2021**, *143* (38), 15661-15673.
81. Ghosh, I.; Ghosh, T.; Bardagi, J. I.; König, B., *Science* **2014**, *346* (6210), 725-728.
82. Heredia, M. D.; Puiatti, M.; Rossi, R. A.; Budén, M. E., *Org. Biomol. Chem.* **2022**, *20* (1), 228-239.
83. Kubo, T.; Katoh, C.; Yamada, K.; Okano, K.; Tokuyama, H.; Fukuyama, T., *Tetrahedron* **2008**, *64* (49), 11230-11236.
84. Tanji, Y.; Mitsutake, N.; Fujihara, T.; Tsuji, Y., *Angew. Chem. Int. Ed.* **2018**, *57* (32), 10314-10317.
85. Shan, X.-H.; Yang, B.; Qu, J.-P.; Kang, Y.-B., *Chem. Commun.* **2020**, *56* (29), 4063-4066.
86. Constantin, T.; Juliá, F.; Sheikh, N. S.; Leonori, D., *Chem. Sci.* **2020**, *11* (47), 12822-12828.
87. Constantin, T.; Zanini, M.; Regni, A.; Sheikh, N. S.; Juliá, F.; Leonori, D., *Science* **2020**, *367* (6481), 1021-1026.